이학박사 학위논문

Numerical simulation of cavity flow by using conforming and nonconforming finite elements

순응 및 비순응 유한요소를 이용한 공동 구조에서의
유체 유동 수치 해석

2014 년 8 월

서울대학교 대학원

협동과정 계산과학 전공

임 록 택

Numerical simulation of cavity flow by using conforming and nonconforming finite elements

순응 및 비순응 유한요소를 이용한 공동 구조에서의 유체 유동 수치 해석

지도교수 신 동 우

이 논문을 이학박사 학위논문으로 제출함

2014 년 6 월

서울대학교 대학원

협동과정 계산과학 전공

임 록 택

임 록 택의 이학박사 학위논문을 인준함

2014 년 6 월

위 원 장	정 상 권	(인)
부위원장	신 동 우	(인)
위 원	이 형 천	(인)
위 원	전 영 목	(인)
위 원	김 임 범	(인)
위 원	심 임 보	(인)

Abstract

Numerical simulation of cavity flow by using conforming and nonconforming finite elements

Roktaek Lim
Interdisciplinary Graduate Program Computational Science
Technology
The Graduate School
Seoul National University

This thesis presents a numerical method for solving the incompressible flow in a square cavity without smoothing the corner singularities. Since nonconforming finite element method can avoid vertex degree of freedom, the values at the upper corners of the cavity are not required to solve the problem. By taking this advantage it is possible to compute accurate numerical solution of the cavity flow without any modification of the problem. The stable nonconforming P_1-P_0 pair used to solve the incompressible flow problem. DSSY finite elements are added to elements which are on the top corners in the cavity to obtain a more accurate approximation of the boundary condition. Numerical solutions by using conforming finite element are computed for the purposes of comparison. The numerical results are compared with those in the literature and show good agreement. Numerical results computed by using the stable nonconforming P_1-P_0 pair show excellent accuracy.

Keywords : conforming finite element method, nonconforming finite element method, stable nonconforming P_1-P_0 pair, DSSY finite element, the incom-

pressible Navier-Stokes equations, lid driven cavity problem

Student Number : 2008-20491

Contents

List of Figures

List of Tables

Chapter 1

Introduction

1.1 Motivation

Two pairs of finite element spaces for the stationary incompressible Stokes problem are introduced in [32]. These pairs are based on square mesh. The finite element space for the velocity field is composed of the P_1 nonconforming quadrilateral [37] element or added by one additional macro DSSY[16] bubble functions. The pressure field is approximated by the piecewise constant function. The stability and optimal convergence results for these element pairs can be found in [32].

The lid driven square cavity is one of the most popular benchmark problem for new numerical methods for the incompressible Navier-Stokes equations in terms of accuracy, numerical efficiency and so on. The stable nonconforming P_1-P_0 element pair will be employed for solving the lid driven square cavity problem. The presence of singularities in upper corners of the cavity give numerical difficulties for solving the cavity flow problem. It might be dangerous

to use high-order methods without handling of the corner singularities due to Gibbs phenomenon. Many studies have been carried out to overcome this difficulty. Various high-order methods have been employed to control of oscillations near corner singularities. Other studies change the boundary condition to overcome this difficulty. This is the so-called regularized lid driven cavity problem. The constant boundary condition for velocity is replaced by a function that vanishes at the upper corners of cavity [23, 44]. Botella and Peyret [6] solved regularized cavity problem by using a subtraction method of the leading terms of the asymptotic expansion of the solution of the Navier-Stokes equations in the vicinity of the corners, where the velocity is discontinuous. Sahin and Owens [42] insert leaks across the heights of the finite volumes in the corners between lid and the vertical walls to handle corner singularities.

We try to solve the lid driven cavity problem without any modification. A numerical method is presented for solving the incompressible flow in a square cavity without regularizing the boundary condition on the top of the cavity. When the nonconforming finite element is used to solve the lid driven cavity problem, we do not consider values at the upper corners in the square cavity. Implementation method for this will be described in Section 4.3. We solve the lid driven cavity problem with unregularized boundary condition by using the stable nonconforming P_1-P_0 finite element. Numerical solutions by using conforming finite element, Q_2-Q_1, are computed for the purposes of comparison. Indicators to check accuracy of the numerical solutions will be presented in this thesis. Numerical solutions of steady steady incompressible flow in a square cavity will be presented Section 4.4.

1.2 Model equations

In this section we shall briefly derive equations governing the motion of an incompressible Newtonian fluid. The governing equations of incompressible Newtonian fluid are derived from the conservation of mass, momentum, and energy. We denoted by $\mathbf{u}(\mathbf{x}, t)$ the velocity of the fluid and $\rho(\mathbf{x}, t)$ the density.

Conservation of mass   Consider a domain Ω in the fluid which is fixed in space and time in an Euclidean coordinate system, a closed surface Γ which enclose Ω, and the unit vector $\mathbf{n}$ normal to Γ pointing from inside of Ω to outside. The conservation of mass states that the rate of change of mass in Ω equals the amount of fluid flowing through Γ. Then, we have

$$\int_\Omega \frac{\partial \rho}{\partial t} \, d\Omega + \int_\Gamma \rho \mathbf{u} \cdot \mathbf{n} \, d\Gamma. \tag{1.1}$$

Applying the divergence theorem to the surface integral in (1.1), (1.1) can be written

$$\int_\Omega \frac{\partial \rho}{\partial t} + \nabla \cdot (\rho \mathbf{u}) \, d\Omega = 0. \tag{1.2}$$

(1.2) is the integral form of mass conservation. Since Ω can be arbitrary,

$$\frac{\partial \rho}{\partial t} + \nabla \cdot (\rho \mathbf{u}) = 0. \tag{1.3}$$

(1.3) implies that

$$\frac{\partial \rho}{\partial t} + \mathbf{u} \cdot \nabla \rho + \rho \nabla \cdot \mathbf{u} = 0. \tag{1.4}$$

The material derivative is defined as

$$\frac{D}{Dt} = \frac{\partial}{\partial t} + \mathbf{u} \cdot \nabla \tag{1.5}$$

3

where $\mathbf{u}$ is the velocity of the fluid. Then (1.4) can be written

$$\frac{D\rho}{Dt} + \rho \nabla \cdot \mathbf{u} = 0. \tag{1.6}$$

(1.3) and (1.6) are referred to as the continuity equation. If the fluid is incompressible, the density ρ is constant with respect to both space and time, $\frac{D\rho}{Dt} = 0$ and the continuity equation reduced to

$$\nabla \cdot \mathbf{u} = 0 \tag{1.7}$$

which is the incompressible condition for the fluid.

Conservation of momentum Conservation of momentum is implied by Newton's second law $\mathbf{F} = \frac{d\mathbf{p}}{dt}$, where $\mathbf{p} = m\mathbf{v}$ is momentum. The conservation of momentum states that the rate of change of momentum in Ω plus the flux of momentum out through Γ is equal to the rate of change of momentum due to body forces and surface stresses. Then, we have

$$\frac{\partial}{\partial t} \int_{\Omega} \rho \mathbf{u} \, d\Omega + \int_{\Gamma} \rho \mathbf{n} \cdot \mathbf{u}\mathbf{u} \, d\Gamma = \int_{\Omega} \rho \mathbf{f} \, d\Omega + \int_{\Gamma} \sigma \cdot \mathbf{n} \, d\Gamma \tag{1.8}$$

where $\mathbf{f}$ is body force and σ is the stress tensor, $\mathbf{u}\mathbf{u}$ represents for the dyadic product. Applying the divergence theorem to the surface integral in (1.8), (1.8) can be written

$$\int_{\Omega} \frac{\partial}{\partial t} \rho \mathbf{u} + \nabla \cdot (\rho \mathbf{u}\mathbf{u}) \, d\Omega = \int_{\Omega} \rho \mathbf{f} + \nabla \cdot \sigma \, d\Omega. \tag{1.9}$$

Since Ω can be arbitrary, we have

$$\frac{\partial}{\partial t} \rho \mathbf{u} + \nabla \cdot (\rho \mathbf{u}\mathbf{u}) = \rho \mathbf{f} + \nabla \cdot \sigma. \tag{1.10}$$

And (1.10) implies that

$$\rho\frac{\partial \mathbf{u}}{\partial t} + \mathbf{u}\frac{\partial \rho}{\partial t} + \rho\mathbf{u}\cdot\nabla\mathbf{u} + \mathbf{u}\nabla\cdot(\rho\mathbf{u}) = \rho\mathbf{f} + \nabla\cdot\sigma. \qquad (1.11)$$

For Newtonian fluids, the constitutive relationship for the stress tensor σ is given by Newton's law,

$$\begin{aligned}
\sigma &= -pI + \tau, \\
\tau &= \lambda(\nabla\cdot\mathbf{u})I + 2\mu\epsilon, \qquad\qquad (1.12) \\
\epsilon &= \frac{1}{2}\left[\nabla\mathbf{u} + (\nabla\mathbf{u})^T\right],
\end{aligned}$$

where p is the pressure, μ is the coefficient of dynamic viscosity, λ is the second coefficient of viscosity, ϵ is the strain tensor. If the fluid is incompressible and homogeneous, then μ and λ are constant and $\epsilon = \nabla\mathbf{u}$. Also using the incompressible condition, we can obtain

$$\nabla\cdot\sigma = -\nabla p + \mu\triangle\mathbf{u}. \qquad (1.13)$$

Then, (1.11) can be written

$$\frac{\partial\mathbf{u}}{\partial t} + \mathbf{u}\cdot\nabla\mathbf{u} = -\frac{1}{\rho}\nabla p + \nu\triangle\mathbf{u} + \mathbf{f} \qquad (1.14)$$

where $\nu = \mu/\rho$ is the kinematic viscosity. (1.14) is the governing equation in fluid dynamics, known as the Navier-Stokes equation.

Conservation of energy The conservation of energy states that the rate of change of energy in Ω plus the flux of energy out through Γ is equal to the flux of heat in through Γ plus the rate of change of energy due to surface

stresses. Then, we have

$$\frac{\partial}{\partial t} \int_\Omega \rho E \, d\Omega + \int_\Gamma \rho E (\mathbf{u} \cdot \mathbf{n}) \, d\Gamma = -\int_\Gamma \mathbf{q} \cdot \mathbf{n} \, d\Gamma + \int_\Gamma (\sigma \cdot \mathbf{u}) \cdot \mathbf{n} \, d\Gamma \qquad (1.15)$$

where $\mathbf{q}$ is heat flux vector. In (1.15), E is the total specific energy given by

$$E = e + \frac{1}{2}\mathbf{u}^2 - \mathbf{f} \cdot \mathbf{u} \qquad (1.16)$$

where e is the specific internal energy, $\frac{1}{2}\mathbf{u}^2$ is the specific kinetic energy, and $-\mathbf{f} \cdot \mathbf{u}$ is the specific potential energy. Applying the divergence theorem to the surface integral in (1.15), (1.15) can be written

$$\int_\Omega \frac{\partial}{\partial t}\rho E + \nabla \cdot (\rho E \mathbf{u}) \, d\Omega = \int_\Omega -\nabla \cdot \mathbf{q} + \nabla \cdot (\sigma \cdot \mathbf{u}) \, d\Omega. \qquad (1.17)$$

Since Ω can be arbitrary, we have

$$\frac{\partial}{\partial t}\rho E + \nabla \cdot (\rho E \mathbf{u}) = -\nabla \cdot \mathbf{q} + \nabla \cdot (\sigma \cdot \mathbf{u}). \qquad (1.18)$$

In this thesis we consider the isothermal fluid. In this case, temperature is uniform in space and time. Hence the energy equation will not mentioned hereafter.

Dimensionless formulation   We have derived the Navier-Stokes equations for incompressible flow,

$$\rho \frac{\partial \mathbf{u}}{\partial t} - \mu \triangle \mathbf{u} + \rho (\mathbf{u} \cdot \nabla)\mathbf{u} + \nabla p = \mathbf{f}, \text{ in } \Omega \times (0, T),$$
$$\nabla \cdot \mathbf{u} = 0, \text{ in } \Omega \times (0, T) \qquad (1.19)$$

with boundary condition

$$\mathbf{u} = \mathbf{w} \ \ \text{on} \ \ \partial\Omega_D, \ \ \nu\frac{\partial\mathbf{u}}{\partial n} - \mathbf{n}p = \mathbf{s} \ \ \text{on} \ \ \partial\Omega_N \ .$$

We can obtain the following dimensionless formulation by introducing $\mathbf{u} = V\widehat{\mathbf{u}}$, $\mathbf{x} = L\widehat{\mathbf{x}}$, $t = L/V\widehat{t}$, $p = V^2\rho\widehat{p}$, and $\mathbf{f} = V^2/L\widehat{\mathbf{f}}$ with a characteristic velocity V and a characteristic length L,

$$
\begin{aligned}
\frac{\partial\widehat{\mathbf{u}}}{\partial\widehat{t}} - \widehat{\nu}\triangle\widehat{\mathbf{u}} + (\widehat{\mathbf{u}} \cdot \widehat{\nabla})\widehat{\mathbf{u}} + \widehat{\nabla}\widehat{p} &= \widehat{\mathbf{f}}, \ \text{in} \ \Omega \times (0, T), \\
\widehat{\nabla} \cdot \widehat{\mathbf{u}} &= 0, \ \text{in} \ \Omega \times (0, T),
\end{aligned}
\tag{1.20}
$$

where

$$\widehat{\nu} = \frac{1}{\text{Re}} = \frac{\mu}{\rho L V},$$

with the dimensionless Reynolds number Re. The boundary conditions on $\partial\Omega = \partial\Omega_D \cup \partial\Omega_N$ are given by

$$\widehat{\mathbf{u}} = \widehat{\mathbf{w}} \ \ \text{on} \ \ \partial\Omega_D, \ \ \nu\frac{\partial\widehat{\mathbf{u}}}{\partial\widehat{n}} - \widehat{\mathbf{n}}\widehat{p} = \widehat{\mathbf{s}} \ \ \text{on} \ \ \partial\Omega_N \ .$$

For simplicity in notation we will omit hats in (1.20). Dropping the convection term $(\mathbf{u} \cdot \nabla)\mathbf{u}$ and setting $\frac{\partial\mathbf{u}}{\partial t} = 0$ gives the stationary Stokes equations

$$
\begin{aligned}
-\nu\triangle\mathbf{u} + \nabla p &= \mathbf{f}, \ \text{in} \ \Omega, \\
\nabla \cdot \mathbf{u} &= 0, \ \text{in} \ \Omega,
\end{aligned}
\tag{1.21}
$$

with boundary conditions

$$\mathbf{u} = \mathbf{w} \ \ \text{on} \ \ \partial\Omega_D, \ \ \nu\frac{\partial\mathbf{u}}{\partial n} - \mathbf{n}p = \mathbf{s} \ \ \text{on} \ \ \partial\Omega_N \ .$$

Chapter 2

Preliminaries

2.1 Finite element discretization

We consider numerical solutions of two dimensional incompressible flow in a square domain, then $\Omega = [0, 1]^2$. Set

$$L_0^2(\Omega) = \left\{ q \in L^2(\Omega) \mid \int_\Omega q \, d\mathbf{x} = 0 \right\}. \tag{2.1}$$

Let us denoted by

$$(u, v) = \int_\Omega uv \, dx \tag{2.2}$$

the inner product in $L_0^2(\Omega)$ and by

$$\|v\|_{0,\Omega} = \sqrt{(v, v)} \tag{2.3}$$

the corresponding norm.

Given any integer $m \geq 0$, let

$$H^m(\Omega) = \{v \mid v \in L^2(\Omega), \ \partial^\alpha v \in L^2(\Omega), |\alpha| \leq m\} \tag{2.4}$$

be the usual Sobolev space provided with the norm

$$\|v\|_{m,\Omega} = \left(\sum_{|\alpha| \leq m} \|\partial^\alpha v\|_{0,\Omega}^2 \right)^{1/2}, \tag{2.5}$$

and the seminorm

$$|v|_{m,\Omega} = \left(\sum_{|\alpha| = m} \|\partial^\alpha v\|_{0,\Omega}^2 \right)^{1/2}. \tag{2.6}$$

Let

$$H_0^1 = \left\{ v \in H^1(\Omega) \mid u = 0 \text{ on } \partial\Omega_D \right\}. \tag{2.7}$$

Let $[L^2(\Omega)]^N$ and $[H^m(\Omega)]^N$ be the space of vector functions $\mathbf{v} = (v_1, \ldots, v_N)$ with components v_j in $L^2(\Omega)$ and $H^m(\Omega)$. The inner product in $[L^2(\Omega)]^N$ is given by

$$(\mathbf{u}, \mathbf{v}) = \int_\Omega \mathbf{u} \cdot \mathbf{v}. \tag{2.8}$$

Let

$$\mathbf{H}_0^1 = \left\{ \mathbf{u} \in [H^1(\Omega)]^2 \mid \mathbf{u} = \mathbf{0} \text{ on } \partial\Omega_D \right\}. \tag{2.9}$$

Bilinear forms $a(\cdot, \cdot) \ : \ \mathbf{H}^1 \times \mathbf{H}^1 \to \mathbb{R}$ and $b(\cdot, \cdot) \ : \ \mathbf{H}^1 \times L_0^2(\Omega) \to \mathbb{R}$, are defined by

$$a(\mathbf{u}, \mathbf{v}) = \nu \int_\Omega \nabla \mathbf{u} : \nabla \mathbf{v} \, d\mathbf{x},$$
$$b(\mathbf{v}, q) = - \int_\Omega q \nabla \cdot \mathbf{v} \, dx. \tag{2.10}$$

Trilinear form $c(\,\cdot\, ; \,\cdot\,,\cdot\,)\ :\ \mathbf{H}^1 \times \mathbf{H}^1 \times \mathbf{H}^1 \to \mathbb{R}$ is defined by

$$c(\mathbf{w}; \mathbf{u}, \mathbf{v}) = \int_\Omega (\mathbf{w} \cdot \nabla)\mathbf{u} \cdot \mathbf{v} \, d\mathbf{x}. \qquad (2.11)$$

The weak formulation of (1.20) with the Dirichlet boundary condition $\mathbf{u} = \mathbf{w}$ on $\partial\Omega_D$ is to find $\mathbf{u} \in \mathbf{H}^1$ and $p \in L_0^2(\Omega)$ such that

$$\left(\frac{\partial\mathbf{u}}{\partial t}, \mathbf{v}\right) + a(\mathbf{u}, \mathbf{v}) + c(\mathbf{u}; \mathbf{u}, \mathbf{v}) + b(\mathbf{v}, p) = (\mathbf{f}, \mathbf{v}), \ \forall \mathbf{v} \in \mathbf{H}_0^1,$$
$$b(\mathbf{u}, q) = 0, \ \forall q \in L_0^2(\Omega). \qquad (2.12)$$

Let $\mathbf{V}_0^h$ and Q^h be the finite dimensional subspace of $\mathbf{H}_0^1$ and $L_0^2(\Omega)$. Then, we can find approximation of $\mathbf{u}_h$ and p_h in the finite dimensional subspaces $\mathbf{V}^h$ and Q^h by solving the following discrete problems:
Find $\mathbf{u}_h \in \mathbf{V}^h$ and $p_h \in Q^h$ such that

$$\left(\frac{\partial\mathbf{u}_h}{\partial t}, \mathbf{v}_h\right) + a(\mathbf{u}_h, \mathbf{v}_h) + c(\mathbf{u}_h; \mathbf{u}_h, \mathbf{v}_h) + b(\mathbf{v}_h, p_h) = (\mathbf{f}, \mathbf{v}_h), \ \forall \mathbf{v}_h \in \mathbf{V}_0^h,$$
$$b(\mathbf{u}_h, q_h) = 0, \ \forall q_h \in Q^h. \qquad (2.13)$$

2.2 The stable nonconforming P_1-P_0 element pair

Two pairs of stable cheapest nonconforming finite element pairs which approximate the stationary Stokes equations are introduced in [32].

2.2.1 The P_1-nonconforming quadrilateral element

We use the approximate space for the velocity is based on the P_1-nonconforming quadrilateral element [37]. Let Q be the general quadrilateral with vertices,

$v_j, j = 1, \ldots, 4$ and the midpoints of edge Q, $m_j, j = 1, \ldots, 4$ such that

$$m_j = \frac{v_{j-1} + v_j}{2}, \ 1 \leq j \leq 4 \qquad (2.14)$$

with identification $v_0 = v_4$. Set $P_1(Q) = \mathrm{Span}\{1, x, y\}$. We recall useful lemma:

Lemma 1 ([37]). *If $u \in P_1(Q)$, then $u(m_1) + u(m_3) = u(m_2) + u(m_4)$. Conversely, if $u_j, j = 1, \ldots, 4$ are given at m_j and satisfy $u_1 + u_3 = u_2 + u_4$, then there exists a unique function $u \in P_1(Q)$ such that $u(m_j) = u_j, j = 1, \ldots, 4$. For $1 \leq j \leq$, let $\widehat{\phi}_j \in P_1(Q)$ be defined such that*

$$\widehat{\phi}_j(m_k) = \begin{cases} 1, & k = j, j + 1, \\ 0, & otherwise. \end{cases} \qquad (2.15)$$

Then $\mathrm{Span}\{\widehat{\phi}_1, \widehat{\phi}_2, \widehat{\phi}_3, \widehat{\phi}_4\} = P_1(Q)$. Indeed, any three of $\widehat{\phi}_1, \widehat{\phi}_2, \widehat{\phi}_3, \widehat{\phi}_4$ span $P_1(Q)$.

According to Lemma 1, $\dim(P_1(Q)) = 3$ and any three of $\widehat{\phi}_1, \widehat{\phi}_2, \widehat{\phi}_3, \widehat{\phi}_4$ form a local basis for the P_1-nonconforming quadrilateral element space.

Let $\mathcal{T}_h$ be a family of regular partition of Ω into disjoint quadrilaterals $Q_j, j = 1, \ldots, N_Q$. The global basis functions of $\mathcal{NC}_0^h(\Omega)$ is defined by

$$\mathcal{NC}_0^h = \{v \in L^2(\Omega) \mid v|_{Q_j} \in P_1(Q_j) \ \forall Q_j \in \mathcal{T}_h, \ v \text{ is continuous at}$$

the mid point of each interior edge in $\mathcal{T}_h$ and v vanishes at

the mid point of each boundary edge in $\mathcal{T}_h\}$,

The global basis functions of $\mathcal{NC}_0^h(\Omega)$ can be defined vertex-wise. $\phi_j \in \mathcal{NC}_0^h(\Omega)$ for each interior vertex (x_j, y_j) is defined such that it has value 1 at the midpoint of each interior edge whose end points contain their vertex (x_j, y_j) and value 0 at the midpoint of every other edge in $\mathcal{T}_h$.

In this thesis, we only consider square domain and uniform and square mesh with $h = 1/N$. Then, Q is the square with size $h \times h$. And $\widehat{\phi}_j$ which are define on $Q_j \in \mathcal{T}_h$ with center of Q_j, $(c_{x,j}, c_{y,j})$ have the form

$$
\begin{aligned}
\widehat{\phi}_1 &= \frac{1}{2} - \frac{c_{x,j}}{h} - \frac{c_{y,j}}{h} + \frac{x}{h} + \frac{y}{h}, \\
\widehat{\phi}_2 &= \frac{1}{2} + \frac{c_{x,j}}{h} - \frac{c_{y,j}}{h} - \frac{x}{h} + \frac{y}{h}, \\
\widehat{\phi}_3 &= \frac{1}{2} - \frac{c_{x,j}}{h} - \frac{c_{y,j}}{h} - \frac{x}{h} - \frac{y}{h}, \\
\widehat{\phi}_3 &= \frac{1}{2} - \frac{c_{x,j}}{h} + \frac{c_{y,j}}{h} + \frac{x}{h} - \frac{y}{h}.
\end{aligned}
\tag{2.16}
$$

2.2.2 The piecewise constant element

The approximate space for the pressure is the piecewise constant element,

$$
P^h = \{ q \in L_0^2(\Omega) \mid q|_Q \in P_0(Q) \ \forall Q \in \mathcal{T}_h \},
$$

where $P_0(A)$ denotes the space of piecewise constants on the set A. The $([\mathcal{NC}_0^h]^2, P^h)$ approximation is unstable[34]. In [32], the stable pair of spaces $([\mathcal{NC}_0^h]^2, P_{cf}^h)$ is proposed. P_{cf}^h is removed a global checkerboard pattern from P^h.

A example of P_{cf}^h is the following. $\mathcal{T}_h$ is treated as a checkerboard with red and black squares. Let $R = \{ Q_{R_1}, \ldots, Q_{R_{N_Q/2}} \}$ and $B = \{ Q_{B_1}, \ldots, Q_{B_{N_Q/2}} \}$ be the set of red and black squares such that $R \cup B = \mathcal{T}_h$. Let ψ_k be the basis

Table 2.1: Number of degrees of freedom for different pairs (velocity/pressure)

N	Q_2-Q_1	Q_2-P_0	Rotated Q_1-P_0	Stable P_1^{NC}-P_0
2^4	2178/289	2178/256	1088/256	450/254
2^5	8450/1089	8450/1024	4224/1024	1922/1022
2^6	33282/4225	33282/4096	16640/4096	7938/4094
2^7	132098/16641	132098/16384	66048/16384	32256/16382

function of P_{cf}^h. Then,

$$
\psi_k(\mathbf{x}) = \begin{cases} 1, & \mathbf{x} \in Q_{R_k} \\ -1, & \mathbf{x} \in Q_{R_{k+1}} \\ 0, & \text{otherwise} \end{cases} \quad \text{for } k = 1, \dots, \frac{N_Q}{2} - 1,
$$

$$
\psi_{N_Q/2-1+k}(\mathbf{x}) = \begin{cases} 1, & \mathbf{x} \in Q_{B_k} \\ -1, & \mathbf{x} \in Q_{B_{k+1}} \\ 0, & \text{otherwise} \end{cases} \quad \text{for } k = 1, \dots, \frac{N_Q}{2} - 1.
$$

(2.17)

For details see [32].

2.2.3 The stable cheapest finite element pair

There are several stable quadrilateral finite element pairs satisfying the inf-sup condition [15, 31, 38]. Table 2.1 shows Number of degrees of freedom for different pairs. The stable nonconforming P_1-P_0 element pair has the lowest number of degrees freedom. The dimension of the pair of spaces $([\mathcal{NC}_0^h]^2, P_{cf}^h)$ is $2N_v^i + N_Q - 2$. N_v^i is the number of interior vertices in $\mathcal{T}_h$. Let stable P_1^{NC}-P_0 denote the stable nonconforming P_1-P_0.

Chapter 3

Numerical methods for the discretized Navier-Stokes problems

We are interested in steady state solutions of lid driven square cavity flow with various Reynolds numbers. Setting $\frac{\partial \mathbf{u}}{\partial t} = 0$ in (1.20) gives the steady state incompressible Navier-Stokes,

$$
\begin{aligned}
-\nu \triangle \mathbf{u} + (\mathbf{u} \cdot \nabla)\mathbf{u} + \nabla p = \mathbf{f}, \ \text{in} \ \Omega, \\
\nabla \cdot \mathbf{u} = 0, \ \text{in} \ \Omega,
\end{aligned}
\tag{3.1}
$$

with boundary conditions

$$
\mathbf{u} = \mathbf{w} \ \ \text{on} \ \ \partial\Omega_D, \ \nu\frac{\partial \mathbf{u}}{\partial n} - \mathbf{n}p = \mathbf{s} \ \ \text{on} \ \ \partial\Omega_N \ .
$$

We only consider the incompressible Navier-Stokes equations with Dirichlet boundary condition in this thesis.

The weak formulation of (3.1) is to find $\mathbf{u} \in \mathbf{H}^1$ and $p \in L_0^2(\Omega)$ such that

$$a(\mathbf{u}, \mathbf{v}) + c(\mathbf{u}; \mathbf{u}, \mathbf{v}) + b(\mathbf{v}, p) = (\mathbf{f}, \mathbf{v}), \ \forall \mathbf{v} \in \mathbf{H}_0^1,$$
$$b(\mathbf{u}, q) = 0, \ \forall q \in L_0^2(\Omega). \tag{3.2}$$

Solving (3.2) requires nonlinear iteration with linearized problem. Given initial guess $(\mathbf{u}^{(0)}, p^{(0)}) \in \mathbf{H}^1 \times L_0^2(\Omega))$, a sequence of iterates

$$(\mathbf{u}^{(1)}, p^{(1)}), (\mathbf{u}^{(2)}, p^{(2)}), \ldots \in \mathbf{H}^1 \times L_0^2(\Omega)$$

is computed which converges to the solution of the weak formulation (3.2). The nonlinear residual of the k-th iterate $(\mathbf{u}^{(k)}, p^{(k)})$ is produced by

$$r_v^{(k)} = (\mathbf{f}, \mathbf{v}) - a(\mathbf{u}^{(k)}, \mathbf{v}) - c(\mathbf{u}^{(k)}; \mathbf{u}^{(k)}, \mathbf{v}) - b(\mathbf{v}, p^{(k)}), \ \forall \mathbf{v} \in \mathbf{H}_0^1,$$
$$r_p^{(k)} = -b(\mathbf{u}^{(k)}, q), \ \forall q \in L_0^2(\Omega). \tag{3.3}$$

Let $\mathbf{u} = \mathbf{u}^{(k)} + \delta\mathbf{u}^{(k)}$ and $p = p^{(k)} + \delta p^{(k)}$ be the solution of (3.2). Since $\delta\mathbf{u}^{(k)} \in \mathbf{H}_0^1$ and $\delta p^{(k)} \in L_0^2(\Omega)$, it follows that

$$r_v^{(k)} = c(\delta\mathbf{u}^{(k)}; \delta\mathbf{u}^{(k)}, \mathbf{v}) + c(\delta\mathbf{u}^{(k)}; \mathbf{u}^{(k)}, \mathbf{v}) + c(\mathbf{u}^{(k)}; \delta\mathbf{u}^{(k)}, \mathbf{v})$$
$$+ a(\delta\mathbf{u}^{(k)}, \mathbf{v}) + b(\mathbf{v}, \delta p^{(k)}), \ \forall \mathbf{v} \in \mathbf{H}_0^1, \tag{3.4}$$
$$r_p^{(k)} = b(\delta\mathbf{u}^{(k)}, q), \ \forall q \in L_0^2(\Omega).$$

After dropping the quadratic term in (3.4) we can obtain the following linear problem:

Find $\delta\mathbf{u}^{(k)} \in \mathbf{H}_0^1$ and $\delta p^{(k)} \in L_0^2(\Omega)$ such that

$$
\begin{aligned}
r_v^{(k)} &= c(\delta\mathbf{u}^{(k)}; \mathbf{u}^{(k)}, \mathbf{v}) + c(\mathbf{u}^{(k)}; \delta\mathbf{u}^{(k)}, \mathbf{v}) \\
&\quad + a(\delta\mathbf{u}^{(k)}, \mathbf{v}) + b(\mathbf{v}, \delta p^{(k)}), \ \forall \mathbf{v} \in \mathbf{H}_0^1, \\
r_p^{(k)} &= b(\delta\mathbf{u}^{(k)}, q), \ \forall q \in L_0^2(\Omega).
\end{aligned}
\tag{3.5}
$$

(3.5) is referred as Newton correction. The discrete form of (3.5) is to find corrections $\delta\mathbf{u}_h^{(k)} \in \mathbf{V}^h$ and $\delta p_h^{(k)} \in Q^h$ such that

$$
\begin{aligned}
r_v^{(k)} &= c(\delta\mathbf{u}_h^{(k)}; \mathbf{u}_h^{(k)}, \mathbf{v}_h) + c(\mathbf{u}_h^{(k)}; \delta\mathbf{u}_h^{(k)}, \mathbf{v}_h) \\
&\quad + a(\delta\mathbf{u}_h^{(k)}, \mathbf{v}_h) + b(\mathbf{v}_h, \delta p_h^{(k)}), \ \forall \mathbf{v}_h \in \mathbf{V}_0^h, \\
r_p^{(k)} &= b(\delta\mathbf{u}_h^{(k)}, q_h), \ \forall q_h \in Q^h.
\end{aligned}
\tag{3.6}
$$

(3.6) can be converted into algebraic problems. Let ϕ_j be the basis functions for V_0^h and ψ_j be the basis functions for Q^h. We can represent $\mathbf{u}_h \in \mathbf{V}^h$ by

$$
\mathbf{u}_h = \sum_{j=1}^{N_v} \xi_j \begin{pmatrix} \phi_j \\ 0 \end{pmatrix} + \sum_{j=1}^{N_v} \eta_j \begin{pmatrix} 0 \\ \phi_j \end{pmatrix} + \sum_{j=1}^{N_\partial} \alpha_j \begin{pmatrix} \phi_j \\ 0 \end{pmatrix} + \sum_{j=1}^{N_\partial} \beta_j \begin{pmatrix} \phi_j \\ 0 \end{pmatrix}
$$

where α and β are coefficients for the boundary data on $\partial\Omega_D$. And $p_h \in Q^h$ is written as

$$
p_h = \sum_{j=1}^{N_q} q_j \psi_j.
$$

Then, we have

$$
\begin{pmatrix} \nu A + N + W & B^T \\ B & 0 \end{pmatrix} \begin{pmatrix} \delta\mathbf{u}^{(k)} \\ \delta\mathbf{p}^{(k)} \end{pmatrix} = \begin{pmatrix} \mathbf{r}_v^{(k)} \\ \mathbf{r}_p^{(k)} \end{pmatrix}
\tag{3.7}
$$

where

$$A = \begin{pmatrix} A_x & 0 \\ 0 & A_y \end{pmatrix}, \ [A_x]_{j,k} = \int_\Omega \nabla \phi_j \cdot \nabla \phi_k, \ A_y = A_x,$$

$$B = \begin{pmatrix} B_x & B_y \end{pmatrix}, \ [B_x]_{k,j} = -\int_\Omega \psi_k \frac{\partial \phi_j}{\partial x}, \ [B_y]_{k,j} = -\int_\Omega \psi_k \frac{\partial \phi_j}{\partial y},$$

$$N = \begin{pmatrix} N_x & 0 \\ 0 & N_y \end{pmatrix}, \ W = \begin{pmatrix} W_{xx} & W_{xy} \\ W_{yx} & W_{yy} \end{pmatrix},$$

$$[N_x]_{j,k} = \int_\Omega (\mathbf{u}_h^{(k)} \cdot \nabla \phi_j) \cdot \phi_k, \ N_y = N_x, \quad \text{(3.8)}$$

$$[W_{xx}]_{k,j} = \int_\Omega \frac{\partial u_1^{(k)}}{\partial x} \phi_k \phi_j, \ [W_{xy}]_{k,j} = \int_\Omega \frac{\partial u_1^{(k)}}{\partial y} \phi_k \phi_j,$$

$$[W_{yx}]_{k,j} = \int_\Omega \frac{\partial u_2^{(k)}}{\partial x} \phi_k \phi_j, \ [W_{yy}]_{k,j} = \int_\Omega \frac{\partial u_2^{(k)}}{\partial y} \phi_k \phi_j,$$

$$\mathbf{u}_h^{(k)} = \begin{pmatrix} u_1^{(k)} \\ u_2^{(k)} \end{pmatrix}.$$

The right-hand side vector in (3.7) can be evaluated by using (3.3).

Picard iteration method is derived by dropping both the nonlinear term $c(\delta \mathbf{u}^{(k)}; \delta \mathbf{u}^{(k)}, \mathbf{v})$ and the linear term $c(\delta \mathbf{u}^{(k)}; \mathbf{u}^{(k)}, \mathbf{v})$ in (3.4). Then, we have the following linear problem:

Find $\delta \mathbf{u}^{(k)} \in \mathbf{H}_0^1$ and $\delta p^{(k)} \in L_0^2(\Omega)$ such that

$$a(\delta \mathbf{u}^{(k)}, \mathbf{v}) + c(\mathbf{u}^{(k)}; \delta \mathbf{u}^{(k)}, \mathbf{v}) + b(\mathbf{v}, \delta p^{(k)}) = r_v^{(k)}, \ \forall \mathbf{v} \in \mathbf{H}_0^1,$$
$$b(\delta \mathbf{u}^{(k)}, q) = r_p^{(k)}, \ \forall q \in L_0^2(\Omega). \quad \text{(3.9)}$$

The discrete version of (3.9) is to find $\delta \mathbf{u}_h^{(k)} \in \mathbf{V}^h$ and $\delta p_h^{(k)} \in Q^h$ such that

$$a(\delta \mathbf{u}_h^{(k)}, \mathbf{v}_h) + c(\mathbf{u}_h^{(k)}; \delta \mathbf{u}_h^{(k)}, \mathbf{v}_h) + b(\mathbf{v}_h, \delta p_h^{(k)}) = r_v^{(k)}, \ \forall \mathbf{v}_h \in \mathbf{V}^h,$$
$$b(\delta \mathbf{u}_h^{(k)}, q_h) = r_p^{(k)}, \ \forall q_h \in Q^h. \quad \text{(3.10)}$$

17

Solving (3.10) gives the Picard correction. We can also have the system of linear equations corresponding to (3.9),

$$\begin{pmatrix} \nu A + N & B^T \\ B & 0 \end{pmatrix} \begin{pmatrix} \delta \mathbf{u}^{(k)} \\ \delta \mathbf{p}^{(k)} \end{pmatrix} = \begin{pmatrix} \mathbf{r}_v^{(k)} \\ \mathbf{r}_p^{(k)} \end{pmatrix}. \tag{3.11}$$

Substituting $\delta \mathbf{u}^{(k)} = \mathbf{u}^{(k+1)} - \mathbf{u}^{(k)}$ and $\delta p^{(k)} = p^{(k+1)} - p^{(k)}$ into (3.9) gives the following problem:

Find $\delta \mathbf{u}^{(k+1)} \in \mathbf{H}^1$ and $\delta p^{(k+1)} \in L_0^2(\Omega)$ such that

$$a(\mathbf{u}^{(k+1)}, \mathbf{v}) + c(\mathbf{u}^{(k)}; \mathbf{u}^{(k+1)}, \mathbf{v}) + b(\mathbf{v}, \delta p^{(k+1)}) = (\mathbf{f}, \mathbf{v}), \ \forall \mathbf{v} \in \mathbf{H}_0^1,$$
$$b(\mathbf{u}^{(k+1)}, q) = 0, \ \forall q \in L_0^2(\Omega). \tag{3.12}$$

This is the Oseen problem. Also we have the system of linear equations for (3.12)

$$\begin{pmatrix} \nu A + N & B^T \\ B & 0 \end{pmatrix} \begin{pmatrix} \mathbf{u}^{(k+1)} \\ \mathbf{p}^{(k+1)} \end{pmatrix} = \begin{pmatrix} \mathbf{f} \\ \mathbf{g} \end{pmatrix}. \tag{3.13}$$

The solution of the Stokes problem can be used as an initial guess for both Newton and Picard correction. The solution of the Stokes problem can be obtained by solving

$$\begin{pmatrix} \nu A & B^T \\ B & 0 \end{pmatrix} \begin{pmatrix} \mathbf{u} \\ \mathbf{p} \end{pmatrix} = \begin{pmatrix} \mathbf{f} \\ \mathbf{g} \end{pmatrix}. \tag{3.14}$$

Newton's method gives quadratic convergence whereas Picard's method gives linear convergence. The radius of convergence of Newton's method is proportional to the viscosity parameter ν [18]. For high Reynolds numbers, Newton's method does not converge due to a bad initial guess. On the other hand, Picard's method has a much larger radius of convergence [30]. Picard's method can be used to obtain a good initial guess.

3.1 Iterative solvers

The numerical solutions of the incompressible Navier-Stokes problem can be obtain by solving linear systems such as (3.7), (3.11). Solving (3.14) gives an initial guess for the Newton or Picard correction. (3.7), (3.11), and (3.14) are linear systems with saddle point structure.

In this section we briefly review iterative solvers for large and sparse linear systems with saddle point structure.

3.1.1 Krylov subspace methods

Suppose we have the following linear system

$$A\mathbf{x} = \mathbf{b} \tag{3.15}$$

where A is a nonsingular square matrix and $\mathbf{b}$ is given. The j-th Krylov subspace $\mathcal{K}_j$ is

$$\mathcal{K}_j(A, \mathbf{b}) = \text{span}\{\mathbf{b}, A\mathbf{b}, \dots, A^{j-1}\mathbf{b}\}. \tag{3.16}$$

The Krylov subspace methods for solving $A\mathbf{x} = \mathbf{b}$ is to find an approximate solution $\mathbf{x}_k$ from affine subspace $\mathbf{x}_0 + \mathcal{K}_k(A, \mathbf{r}_0)$ where $\mathbf{r}_0 = \mathbf{b} - A\mathbf{x}_0$. There are two different classes

- The minimum residual approach

$$\min_{\mathbf{x}_k \in \mathbf{x}_0 + \mathcal{K}_k(A, \mathbf{r}_0)} \|\mathbf{b} - A\mathbf{x}_k\|.$$

- The orthogonal residual approach

$$\mathbf{x}_k \in \mathbf{x}_0 + \mathcal{K}_k(A, \mathbf{r}_0) \text{ and } (\mathbf{b} - A\mathbf{x}_k) \perp \mathcal{L}_k$$

$$(\mathcal{L}_k \text{ suitable subspace of dimension } k)$$

19

Algorithm 1 Preconditioned GMRES, $A\mathbf{x} = \mathbf{b}$ with preconditioner M

1: Compute $\mathbf{r}_0 = \mathbf{b} - A\mathbf{x}_0$ and $\mathbf{z}_0 = M^{-1}\mathbf{r}_0$
2: $\beta = \|\mathbf{z}_0\|_2$ and $\mathbf{v}_1 = \mathbf{z}_0/\beta$
3: Set $\mathbf{d}_1 = -\mathbf{q}_1 = B\mathbf{u}_1 - \mathbf{g}$
4: **for** $j = 1, 2, \ldots$ until m **do**
5:      Compute $\mathbf{w}_j = M^{-1}A\mathbf{v}_j$
6:      **for** $i = 1, 2, \ldots$ until j **do**
7:          $h_{i,j} = (\mathbf{w}_j, \mathbf{v}_i)$
8:          $\mathbf{w}_j = \mathbf{w}_j - h_{i,j}\mathbf{v}_i$
9:      **end for**
10:     $h_{j+1,j} = \|\mathbf{w}_j\|_2$. If $h_{j+1,j} = 0$, set $m = j$ and go to 13
11:     $\mathbf{v}_{j+1} = \mathbf{w}_j/h_{j+1,j}$
12: **end for**
13: Define the $(m+1) \times m$ Hessenberg matrix $\bar{H}_m = \{h_{i,j}\}_{1 \leq i \leq m+1, 1 \leq j \leq m}$
14: Compute $\mathbf{y}_m$ the minimizer of $\|\beta\mathbf{e}_1 - \bar{H}_m\mathbf{y}_m\|_2$
15: $\mathbf{x}_m = \mathbf{x}_0 + V_m\mathbf{y}_m$ where $V_m = [\mathbf{v}_1 \cdots \mathbf{v}_m]$

GMRES and MINRES method are based on the minimum residual approach. CG, BiCG, and QMR are based on the orthogonal residual approach. $\mathcal{L}_k = \mathcal{K}_k(A, \mathbf{r}_0)$ for CG and $\mathcal{L}_k = \mathcal{K}_k(A^T, \mathbf{r}_0)$ for BiCG and QMR.

MINRES/GMRES   The general minimum residual (GMRES) is introduced in [41]. GMRES is generalization of the MINRES method. GMRES is to find approximate solution $\mathbf{x}_m$ by solving the following least square problem: Find $\mathbf{y} \in \mathbb{R}^m$ such that

$$\min \|\mathbf{b} - A(\mathbf{x}_0 + V_k\mathbf{y}_m)\|_2.$$

This method is based on long recurrences and satisfies an optimal property. GMRES is a stable method and no breakdown occurs. When $h_{j+1,j} = 0$ at step j, the residual vector is zero. This means $\mathbf{x}_j$ has reached the solution [40]. When number of iteration increases, the work per iteration and memory requirements increase. In order to avoid this disadvantage, the restarted GMRES is used in practice.

Algorithm 2 Preconditioned MINRES, $A\mathbf{x} = \mathbf{b}$ with preconditioner M

1: $\mathbf{v}_0 = 0$, $\mathbf{w}_0 = \mathbf{w}_1 = 0$
2: Compute $\mathbf{v}_1 = \mathbf{b} - A\mathbf{x}_0$ and $\mathbf{z}_1 = M^{-1}\mathbf{v}_1$
3: $\gamma_1 = \sqrt{(\mathbf{z}_1, \mathbf{v}_1)}$, $\eta_1 = \gamma_1$ $\gamma_0 = 1$
4: $s_0 = s_1 = 0$, $c_0 = c_1 = 1$
5: **for** $j = 1, 2, \dots$ until $\|\mathbf{b} - A\mathbf{x}_j\|_2 / \|\mathbf{b}\|_2 < TOL$ **do**
6:     $\mathbf{z}_j = \mathbf{z}_j / \gamma_j$
7:     $\delta_j = (A\mathbf{z}_j, z_j)$
8:     $\mathbf{v}_{j+1} = A\mathbf{z}_j - (\delta_j/\gamma_j)\mathbf{v}_j - (\gamma_j/\gamma_{j-1})\mathbf{v}_{j-1}$
9:     $\mathbf{z}_{j+1} = M^{-1}\mathbf{v}_{j+1}$
10:     $\gamma_{j+1} = \sqrt{(\mathbf{z}_{j+1}, \mathbf{v}_{j+1})}$
11:     $a_0 = c_j \delta_j - c_{j-1} s_j \gamma_j$
12:     $a_1 = \sqrt{a_0^2 + \gamma_{j+1}^2}$
13:     $a_2 = s_j \delta_j + c_{j-1} c_j \gamma_j$
14:     $a_3 = s_{j-1} \gamma_j$
15:     $c_{j+1} = a_0/a_1$, $s_{j+1} = \gamma_{j+1}/a_1$
16:     $\mathbf{w}_{j+1} = (\mathbf{z}_{j+1} - a_2 \mathbf{w}_j - a_3 \mathbf{w}_{j-1})/a_1$
17:     $\mathbf{x}_j = \mathbf{x}_{j-1} + c_{j+1} \eta \mathbf{w}_{j+1}$
18:     $\eta = -s_{j+1} \eta$
19: **end for**

When A is symmetric, then the matrix $\bar{H}_m$ reduces to a tridiagonal matrix. This property can be exploited to obtain short recurrence relations. MINRES is optimal solver when A is symmetric and indefinite. The matrix system is positive definite, preconditioned CG is the preferred method.

BiCGstab The stabilized bi-conjugate gradient method (BiCGstab) was introduced in [48]. If A is symmetric positive definite, orthonormal basis of $\mathcal{K}_k(A, \mathbf{r}_0)$ can be computed by using the Lanczos algorithm. The Lanczos algorithm can not be applicable for nonsymmetric matrices. BiCG is based on bi-orthogonal Lanczos algorithm. This algorithm solves the both system $A\mathbf{x} = \mathbf{b}$ and $A^T\mathbf{y} = \mathbf{x}$. BiCG uses a short recurrence for the construction of the orthonormal basis of the Krylov subspace. BiCG requires less memory storage than GMRES. However, BiCG shows irregular convergence in some

Algorithm 3 Preconditioned BiCGstab, $A\mathbf{x} = \mathbf{b}$ with preconditioner M

1: Compute $\mathbf{r}_0 = \mathbf{b} - A\mathbf{x}_0$ and $\mathbf{z}_0 = M^{-1}\mathbf{r}_0$
2: Choose arbitrary $\mathbf{s}_0$ such that $\mathbf{s}_0 \cdot \mathbf{r}_0 \neq 0$, for example $\mathbf{s}_0 = \mathbf{r}_0$
3: $\rho_0 = (\mathbf{s}_0, \mathbf{r}_0)$ and $\mathbf{p}_0 = \mathbf{r}_0$
4: **for** $j = 0, 1, 2, \ldots$ until $\|\mathbf{b} - A\mathbf{x}_j\|_2/\|\mathbf{b}\|_2 < TOL$ **do**
5:     $\mathbf{z}_j = M^{-1}\mathbf{p}_j$
6:     $\alpha = \rho_j/(\mathbf{s}_0, A\mathbf{z}_j)$
7:     $\mathbf{q}_j = \mathbf{r}_j - \alpha A\mathbf{z}_j$
8:     if $\|\mathbf{q}_j\|_2$ is small enough then $\mathbf{x}_{j+1} = \mathbf{x}_j + \alpha\mathbf{z}_j$, quit
9:     $\mathbf{y}_j = M^{-1}\mathbf{q}_j$
10:     $\mathbf{t}_j = A\mathbf{y}_j$
11:     $\omega = (\mathbf{t}_j, \mathbf{q}_j)/(\mathbf{t}_j, bt_j)$
12:     $\mathbf{x}_{j+1} = \mathbf{x}_j + \alpha\mathbf{z}_j + \omega\mathbf{y}_j$
13:     $\mathbf{r}_{j+1} = \mathbf{q}_j - \omega\mathbf{t}_j$
14:     $\rho_{j+1} = (\mathbf{s}_0, \mathbf{r}_{j+1})$
15:     $\beta = (\rho_j/\rho_{j+1})(\alpha/\omega)$
16:     $\mathbf{p}_{j+1} = \mathbf{r}_{j+1} + \beta(\mathbf{p}_j - \omega A\mathbf{z}_j)$
17: **end for**

---

cases. BiCSGstab is developed to remedy this difficulty.

3.1.2   Uzawa method

We consider the solution of the systems of linear equations with saddle-point structure

$$\begin{pmatrix} A & B^T \\ B & 0 \end{pmatrix} \begin{pmatrix} \mathbf{u} \\ \mathbf{p} \end{pmatrix} = \begin{pmatrix} \mathbf{f} \\ \mathbf{g} \end{pmatrix}, \tag{3.17}$$

where

$$A \in \mathbb{R}^{n \times n} \text{ and } B \in \mathbb{R}^{m \times n} \ (n \geq m).$$

First, we assume that A is symmetric positive definite and B is a matrix of full rank. Let $BA^{-1}B^T = S$. A widely known iterative method for (3.17) is

the Uzawa method [8]. The Uzawa method solves the following equations,

$$
\begin{aligned}
A\mathbf{u}_k &= \mathbf{f} - B^T\mathbf{p}_{k-1}, \\
\mathbf{p}_k &= \mathbf{p}_{k-1} + \alpha\left(B\mathbf{u}_k - \mathbf{g}\right),
\end{aligned}
\tag{3.18}
$$

in each iteration. Reformulating the iteration formula (3.18), we can obtain the following relation for $\mathbf{p}_k$,

$$
\mathbf{p}_k = \mathbf{p}_{k-1} + \alpha(BA^{-1}\mathbf{f} - \mathbf{g} - S\mathbf{p}_{k-1}).
\tag{3.19}
$$

This is a Richardson iteration for solving the linear system

$$
BA^{-1}B\mathbf{p} = BA^{-1}\mathbf{f} - \mathbf{g}.
\tag{3.20}
$$

If residue is defined by $\mathbf{r}_k = \mathbf{p} - \mathbf{p}_k$, then

$$
\mathbf{r}_k = (I - \alpha S)^k\mathbf{r}_0.
\tag{3.21}
$$

Since S is symmetric, spectral radius of $I - \alpha S$ is

$$
\rho(I - \alpha S) = \|I - \alpha S\|_2.
\tag{3.22}
$$

Then,

$$
\|\mathbf{r}_k\|_2 = \rho(I - \alpha S)^k\|\mathbf{r}_0\|_2.
\tag{3.23}
$$

Let λ_M and λ_m be the maximum and the minimum eigenvalues of $BA^{-1}B^T$. The Uzawa method is convergent when $0 < \alpha < 2/\lambda_M$. The optimal rate of convergence is obtained with the choice of $\alpha = 2/(\lambda_m + \lambda_M)$. Solving (3.18)

requires the solution of the linear system

$$\mathbf{u}_k = A^{-1}(\mathbf{f} - B^T \mathbf{p}_{k-1}). \qquad (3.24)$$

This operation is expensive and is implemented as an iteration. The inexact Uzawa methods introduced to avoid the calculation of A^{-1} [4, 9]. The linear system in (3.17) can be factored as

$$\begin{pmatrix} A & B^T \\ B & 0 \end{pmatrix} = \begin{pmatrix} A & 0 \\ B & I \end{pmatrix} \begin{pmatrix} A^{-1} & 0 \\ 0 & -S \end{pmatrix} \begin{pmatrix} A & B^T \\ 0 & I \end{pmatrix}. \qquad (3.25)$$

The inexact Uzawa method replaces the matrices A and S in (3.25) by the symmetric positive definite matrices $\widehat{A}$ and $\widehat{S}$. This leads to the approximation of saddle point problem given by

$$\begin{pmatrix} \widehat{A} & 0 \\ B & I \end{pmatrix} \begin{pmatrix} \widehat{A}^{-1} & 0 \\ 0 & -\widehat{S} \end{pmatrix} \begin{pmatrix} \widehat{A} & B^T \\ 0 & I \end{pmatrix} = \begin{pmatrix} \widehat{A} & B^T \\ B & \widehat{C} \end{pmatrix} \qquad (3.26)$$

where $B\widehat{A}^{-1}B^T - \widehat{S} = \widehat{C}$. Then the iterative method for (3.17) can be written as

$$\begin{pmatrix} \mathbf{u}_{k+1} \\ \mathbf{p}_{k+1} \end{pmatrix} = \begin{pmatrix} \mathbf{u}_k \\ \mathbf{p}_k \end{pmatrix} + \begin{pmatrix} \widehat{A} & B^T \\ B & \widehat{C} \end{pmatrix}^{-1} \left\{ \begin{pmatrix} \mathbf{f} \\ \mathbf{g} \end{pmatrix} - \begin{pmatrix} A & B^T \\ B & 0 \end{pmatrix} \begin{pmatrix} \mathbf{u}_k \\ \mathbf{p}_k \end{pmatrix} \right\}. \qquad (3.27)$$

(3.27) gives Algorithm 4.

3.2 Preconditiong

Convergence of Krylov subspace method depends on the spectrum of the linear system. Krylov subspace methods show the best convergence if all eigen-

---
Algorithm 4 Inexact Uzawa method [4]

1: Compute residual $\mathbf{r} = \mathbf{f} - (A\mathbf{u} + B^T\mathbf{p})$ and $\mathbf{s} = \mathbf{g} - B\mathbf{u}$
2: Choose $\widehat{A}$
3: **for** $k = 0, 1, \ldots$ until $\sqrt{\|\mathbf{r}\|_2^2 + \|\mathbf{s}\|_2^2} < \epsilon_{\text{TOL}}$ **do**
4:     Compute $\mathbf{w} = B\widehat{A}^{-1}\mathbf{r} - \mathbf{s}$
5:     Compute an approximate solution $\widehat{\mathbf{z}}$ of linear equation $B\widehat{A}^{-1}B^T\mathbf{z} = \mathbf{w}$
6:     Compute $\mathbf{d} = \widehat{A}^{-1}(\mathbf{r} - B^T\widehat{\mathbf{z}})$
7:     Update $\mathbf{u} = \mathbf{u} + \mathbf{d}$ and $\mathbf{p} = \mathbf{p} + \widehat{\mathbf{z}}$
8: **end for**
---

values are clustered around 1 or away from zero. (3.7), (3.11), and (3.14) are indefinite and the condition numbers of these matrices are large. Therefore, some techniques are required that change the spectrum of (3.7), (3.11), and (3.14).

3.2.1   Algebraic multigrid preconditioner

Multigrid method is one of the most effective iterative solvers for discrete Poisson problems. If multigrid parameters are appropriately chosen, the rate of convergence does not depend on the mesh size h [14, 27, 28].

Also multigrid method can be used as an efficient preconditioner for an iterative solvers. Combining multigrid method with iterative method such as CG, BiCGstab, GMRES is very popular method to solve a system of linear equations. A multigrid preconditioner is a very good preconditioner better than standard one-level ILU-type preconditioner. The major reason is due to the fact that aims at the efficient reduction of all error components, short range as well as long range [46].

In this section, we briefly introduce the multigrid method and the algebraic multigrid method for the P_1-nonconforming quadrilateral element.

Multigrid method   Multigrid methods are based on a sequence of meshes obtained by successive refinement. Suppose we have two level grids Ω_h with width h and Ω_{2h} with width $2h$. Let A_h the second order difference operator defined on Ω_h. A two-level grid method solves the linear systems of equations

$$A_h \mathbf{u}_h = \mathbf{f}_h. \tag{3.28}$$

The basic multigrid consists of two ingredient, smoother and coarse grid correction. Smoother is an iterative method that reduces the fine grid component of the error. Many classical iterative methods, for example, Jacobi, damped Jacobi, Gauss-Seidel, SOR, and so on are effective. Then we need to approximate the error on Ω_h by suitalbe procedure on Ω_{2h}. We need the suitable interpolation operator I_{2h}^h which satisfies

$$I_{2h}^h \mathbf{v}_{2h} = \mathbf{v}_h \in \Omega_h \ , \forall \mathbf{v}_{2h} \in \Omega_{2h} \tag{3.29}$$

and prolongation operator I_h^{2h} which satisfies

$$I_h^{2h} \mathbf{v}_h = \mathbf{v}_{2h} \in \Omega_{2h} \ , \forall \mathbf{v}_h \in \Omega_h. \tag{3.30}$$

Then we can obtain the discrete operator A_{2h} relative to Ω_{2h}

$$A_{2h} = I_h^{2h} A_h I_{2h}^h. \tag{3.31}$$

It is impossible to compute the error in Ω_h, we have to work with residual. Let M be the smoother. For example, we consider Gauss-Seidel smoother, M is lower triangular of A_h. After ν steps the smoothed redsidual $\mathbf{r}^{(\nu)}$ is computed by

$$\mathbf{r}^{(\nu)} = A_h \mathbf{e}^{(\nu)} = A_h (I - M^{-1} A_h)^\nu \mathbf{e}^{(0)}. \tag{3.32}$$

26

Then the smoothed residual to the coarse grid can be written as

$$\tilde{\mathbf{r}} = I_h^{2h}\mathbf{r}^{(\nu)}. \tag{3.33}$$

Since $I_h^{2h}A_h\mathbf{e} = I_h^{2h}\mathbf{r}$, $\mathbf{e} = I_{2h}^h\tilde{\mathbf{e}}$. This gives the coarse grid correction,

$$I_h^{2h}A_hI_{2h}^h\tilde{\mathbf{e}} = \tilde{\mathbf{r}}. \tag{3.34}$$

We can update the solution by using (3.34)

$$\mathbf{u}^{(\nu)} \leftarrow \mathbf{u}^{(\nu)} + I_{2h}^h\tilde{\mathbf{e}}. \tag{3.35}$$

The two-level grid method solves (3.28) by Algorithm 5

Algorithm 5 Two-level grid methods

1: Choose $\mathbf{u}_0$
2: **for** $j = 0, 1, \ldots$ until convergence **do**
3:      Set $\mathbf{u}^{(0)} = \mathbf{u}_j$
4:      Pre-smoothing $\mathbf{u}^{(k)} = (I - M^{-1}A)\mathbf{u}^{(k-1)} + M^{-1}\mathbf{f}_h$, $k = 1, \ldots, \nu$
5:      Compute residual $\mathbf{r}^{(\nu)} = \mathbf{f}_h - A_h\mathbf{u}^{(\nu)}$
6:      $\tilde{r} = I_h^{2h}\mathbf{r}^{(\nu)}$
7:      Compute $\tilde{\mathbf{e}} = A_{2h}^{-1}\tilde{r}$
8:      Update $\tilde{\mathbf{u}} = \mathbf{u}^{(\nu)} + I_{2h}^h\tilde{\mathbf{e}}$, Set $\mathbf{u}^{(0)} = \tilde{\mathbf{u}}$
9:      Post-smoothing $\mathbf{u}^{(k)} = (I - M^{-1}A)\mathbf{u}^{(k-1)} + M^{-1}\mathbf{f}_h$, $k = 1, \ldots, \nu$
10:      $\mathbf{u}_{j+1} = \mathbf{u}^{(\nu)}$
11: **end for**

Algebraic multigrid for the P_1-nonconforming quadrilateral finite element Since the P_1-nonconforming quadrilateral finite element is noncon-forming and $\mathcal{NC}_0^{h-1} \not\subset \mathcal{NC}_0^h$. It is difficult to define the prolongation and interpolation operators. It is possible to describe the algebraic multigrid in the same way as a geometric multigrid by replacing the terms grids, subgrids, and

grid points by set of variables, subsets of variables, and single variables [46]. Thus, AMG(Algebraic Multi Grid) is applicable to the matrix which is generated by nonconforming finite element discretization of the Poisson equation. The application of AMG consists of two processes. The first process is an automatic setup phase splitting the set of variables into a set of coarse variables and a set of fine variables, and defining the interpolation operators. Details can be found [11, 39, 46]. The second process is to compute the approximate solution by performing normal multigrid cycling.

In this thesis, we use Stüben's standard coarsening method to split coarse and fine variables [47]. Consider a linear system, $A_h \mathbf{u}_h = \mathbf{f}_h$. h represents the fine level and H represents the coarse level. Let Ω_h be the index set $\{1, 2, 3, \ldots, n\}$, C be the index set which contains the coarse level indices, and F be the index set which contains the fine level indices. Then, $\Omega_h = C \cup F$, $C \cap F = \emptyset$ and $\Omega_H = C$. Define a variable $j \in \Omega_h$ to be strongly n-coupled to the another variable k, if

$$-(A_h)_{j,k} \geq \epsilon \max_{(A_h)_{j,l} < 0} |(A_h)_{j,l}| \tag{3.36}$$

with $0 < \epsilon 1$. Denote the set of all strong n-couplings of variable j by S_j

$$S_j = \{k \in N_j \mid j \text{ strongly n-coupled to } k\} \tag{3.37}$$

where N_j is neighborhood of a point j defined by

$$N_j = \{k \in \Omega_h \mid k \neq j, \ (A_h)_{j,k} \neq 0\}, \ j \in \Omega_h. \tag{3.38}$$

And introduce the set S_j^T of strong transpose n-couplings of j consisting of all

variables k which are strongly n-coupled to j,

$$S_j^T = \{k \in \Omega_h \mid j \in S_k\}. \tag{3.39}$$

Then, we have the following C/F splitting method Algorithm 6.

Algorithm 6 Standard coarsening method

1: $C = \emptyset$, $F = \emptyset$, $U = \Omega_h$
2: Compute λ_j for $j \in U$
3: **if** $\lambda_j \neq 0$ **then**
4:      Pick $j \in U$ with maximum λ_j, $C = C \cup \{j\}$ and $U = U \backslash \{j\}$
5:      For all $k \in S_j^T \cap U$, $F = F \cup \{k\}$ and $U = U \backslash \{j\}$
6:      Go to 2
7: **end if**
8: $\lambda_j = \left| S_j^T \cap U \right| + 2 \left| S_j^T \cap F \right|$, $j \in U$

To define interpolation, we use Stüben direct interpolation formula. Let

$$C_j = C \cap N_j, \; C_j^s = C \cap S_j,$$
$$F_j = F \cap N_j, \; F_j^s = F \cap S_j. \tag{3.40}$$

For each $j \in F$, we define the set of interpolatory variables by $P_j = C_j^s$ and approximate

$$(A_h)_{j,j} e_j + \alpha_j \sum_{k \in P_j} (A_h)_{j,k} e_k = 0 \tag{3.41}$$

with

$$\alpha_j = \frac{\sum_{k \in N_j} (A_h)_{j,k}}{\sum_{l \in P_j} (A_h)_{j,l}}. \tag{3.42}$$

This leads to the interpolation formula

$$e_j = \sum_{k \in P_j} w_{j,k} e_k \text{ with } w_{j,k} = -\alpha_j \frac{(A_h)_{j,k}}{(A_h)_{j,j}}. \tag{3.43}$$

Since we consider the uniform square mesh with $h = 1/N$, then the Laplacian matrix obtained by the P_1-nonconforming quadrilateral finite element has the form

$$[A_x]_{j,k} = \int_\Omega \nabla\phi_j \cdot \nabla\phi_k = \begin{cases} -2, & k = j - (N-1) - 1, \\ -2, & k = j - (N-1) + 1, \\ 8, & k = j, \\ -2, & k = j + (N-1) - 1, \\ -2, & k = j + (N-1) + 1, \\ 0, & \text{otherwise.} \end{cases} \qquad (3.44)$$

Note that coefficients of A_x are independent of h. We applied Algorithm 6 to A_x with $\epsilon = 0.25$. According to [45], the concrete value of ϵ is not critical in practice and $\epsilon = 0.25$ being a reasonable default value. The coarse and fine splitting result is shown in Figure 3.1.

3.2.2 Block preconditioners for saddle point problems

There is a class of preconditioners that is applied in the form of sub-blocks for the velocity and pressure systems separately. These preconditioners are block preconditioners.

Symmetric case Since νA in (3.14) is symmetric and positive definite, (3.14) can be solved by using MINRES or Uzawa method. Krylov subspace method tends to work well only if appropriate preconditioning is used. In [33], the following theoretical observations are introduced.

Figure 3.1: The finest(black circle) and three consecutive AMG levels created by standard coarsening for $N = 2^4$.
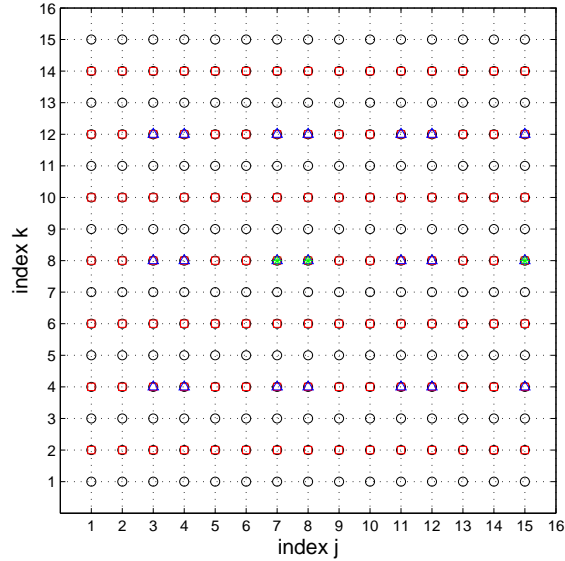
Theorem 2 ([33])**.** *Let*

$$\mathcal{A}\mathbf{u} = \begin{pmatrix} A & B^T \\ C & 0 \end{pmatrix} \begin{pmatrix} \mathbf{x} \\ \mathbf{y} \end{pmatrix} = \begin{pmatrix} \mathbf{f} \\ \mathbf{g} \end{pmatrix}, \tag{3.45}$$

where $A \in \mathbb{R}^{n \times n}$ and $B, C \in \mathbb{R}^{m \times n}$ with $n \geq m$.

If $\mathcal{A}$ is preconditioned by

$$\mathcal{P} = \begin{pmatrix} A & 0 \\ 0 & CA^{-1}B^T \end{pmatrix}, \tag{3.46}$$

then the preconditioned matrix $\mathcal{T} = \mathcal{P}^{-1}\mathcal{A}$ satisfies

$$\mathcal{T}(\mathcal{T} - I)(\mathcal{T}^2 - \mathcal{T} - I) = 0. \tag{3.47}$$

It follows that $\mathcal{T}$ has at most the four distinct eigenvalues $0, 1, \frac{1}{2} \pm \frac{\sqrt{5}}{2}$. If $\mathcal{T}$ is nonsingular then it has the three nonzero eigenvalues.

If consideration of symmetry is not important then a similar argument to the above shows that the choice

$$\mathcal{P} = \begin{pmatrix} A & B^T \\ 0 & CA^{-1}B^T \end{pmatrix} \tag{3.48}$$

yield a preconditioned system with exactly the 2 eigenvalues ± 1.

Also good approximation of A and $BA^{-1}B^T$ are essential when the inexact Uzawa method is used for solving (3.14).

The suggested preconditioner for the Stokes problem is the block diagonal matrix

$$\begin{pmatrix} A_{MG} & \\ 0 & Q \end{pmatrix} \tag{3.49}$$

where A_{MG} is multigrid cycle for the Laplacian and Q is the pressure mass matrix [18]

$$[Q]_{j,k} = \int_\Omega \psi_j \psi_k. \tag{3.50}$$

Also A_{MG} and Q can be used as $\widehat{A}$ and $\widehat{C}$ in Algorithm 4.

We have studied the performance of AMG preconditioner previous section. This preconditioner convergence is independent of h.

Theorem 3 ([18]). *For any Stokes problem with $\partial\Omega = \partial\Omega_D$, discretized using a uniformly stable mixed approximation on a shape regular, quasi-uniform subdivision of $\mathbb{R}^2$, the pressure Schur complement matrix $BA^{-1}B^T$ is spectrally equivalent to the pressure mass matrix Q:*

$$\beta^2 \leq \frac{(BA^{-1}B^T\mathbf{q}, \mathbf{q})}{(Q\mathbf{q}, \mathbf{q})} \leq 1 \ \forall \mathbf{q} \in \mathbb{R}^m. \tag{3.51}$$

32

Table 3.1: Estimated β^2 for Stable P_1^{NC}-P_0

Grid	β^2
$2^4 \times 2^4$	0.2052
$2^5 \times 2^5$	0.1926
$2^6 \times 2^6$	0.1941
$2^7 \times 2^7$	0.1912
$2^8 \times 2^8$	0.1893
$2^9 \times 2^9$	0.1879

Table 3.2: Extremal eigenvalues for the matrix $Q^{-1}BA^{-1}B^T$ for stable P_1^{NC}-P_0 mixed approximation

Grid	$\lambda_{\min}$	$\lambda_{\max}$
$2^4 \times 2^4$	0.2052	1.0000
$2^5 \times 2^5$	0.1926	1.0000
$2^6 \times 2^6$	0.1941	1.0000
$2^7 \times 2^7$	0.1912	1.0000
$2^8 \times 2^8$	0.1893	1.0000
$2^9 \times 2^9$	0.1879	1.0000

β is the inf-sup constant, is bounded away from zero independently of h, and the effective condition number satisfies $\kappa(BA^{-1}B^T) \leq C/(c\beta^2)$, where C and c are the constants given by

$$ch^2 \leq \frac{(Q\mathbf{q}, \mathbf{q})}{(\mathbf{q}, \mathbf{q})} \leq Ch^2 \ \forall \mathbf{q} \in \mathbb{R}^m. \tag{3.52}$$

Theorem 3 states that the eigenvalues of $BA^{-1}B^T$ are bounded below and above by positive constant for the stable discretization of the stationary Stokes problem (1.21). Since (3.51) is independent of mesh size h, if we use (3.49) as a preconditioner for (3.14), then MINRES iteration converges at a rate independent of h.

To illustrate the tightness of the bounds in (3.51), computed extremal eigenvalues for the stable P_1^{NC}-P_0 mixed approximations on a sequence of uniform square grids are given Table 3.2. The upper bound of unity is clearly

tight. Table 3.1 shows the inf-sup eigenvalue seems to be converging to an asymptotic value.

Nonsymmetric case   Since N in (3.7) and (3.11) are nonsymmetric, preconditioned Krylov method such as GMRES or BiCGstab can be used to solve the system of linear equations (3.7) and (3.11). Let

$$F = \nu A + N \text{ or } F = \nu A + N + W. \tag{3.53}$$

The left and right preconditioners are given by

$$\mathcal{P}_R = \begin{pmatrix} F & B^T \\ 0 & \widehat{S} \end{pmatrix}, \ \mathcal{P}_L = \begin{pmatrix} F & 0 \\ B & \widehat{S} \end{pmatrix}, \tag{3.54}$$

where $\widehat{S}$ is an approximation to the Schur complement

$$S = -BF^{-1}B^T.$$

If $\widehat{S} = S$, then

$$\begin{pmatrix} F & B^T \\ B & 0 \end{pmatrix} \mathcal{P}_R^{-1} = \begin{pmatrix} F & B^T \\ B & 0 \end{pmatrix} \begin{pmatrix} F^{-1} & -F^{-1}B^T \widehat{S}^{-1} \\ 0 & \widehat{S}^{-1} \end{pmatrix} = \begin{pmatrix} I & 0 \\ BF^{-1} & I \end{pmatrix} \tag{3.55}$$

and

$$\mathcal{P}_L^{-1} \begin{pmatrix} F & B^T \\ B & 0 \end{pmatrix} = \begin{pmatrix} F^{-1} & 0 \\ -\widehat{S}^{-1}BF^{-1} & \widehat{S}^{-1} \end{pmatrix} \begin{pmatrix} F & B^T \\ B & 0 \end{pmatrix} = \begin{pmatrix} I & F^{-1}B^T \\ 0 & I \end{pmatrix}. \tag{3.56}$$

Thus, the convergence of preconditioned Krylov subspace method is guaranteed in at most 3 iterations [33]. We need a good approximation of the Schur

complement to solve (3.7) and (3.11). Elman [17] suggested the approximation

$$\widehat{S}^{-1} = (BB^T)^{-1} BFB^T (BB^T)^{-1} \approx S \qquad (3.57)$$

is called the least squares commutator preconditioner. Convergence of GMRES iteration is mildly dependent on mesh size and Reynolds number [17].

3.3   Test problems

We made FORTRAN and MATLAB programs which implement the stable P_1^{NC}-P_0 pair for (3.1). Before solving the lid driven square cavity problem, we solved two test problems to validate our programs. We ran our programs on a PC with Intel(R) Core(TM) i5 CPU and 8192 MB RAM.

3.3.1   Algebraic multigrid preconditioner

We first test the performance of the AMG preconditioner for the Laplacian matrix obtained by the P_1-nonconforming quadrilateral finite element. Preconditioned CG is applied to solve the two-dimensional Poisson problem

$$-\triangle u = f, \text{in } \Omega$$
$$u = 0, \text{on } \partial\Omega \qquad (3.58)$$

where $\Omega = [0,1]^2$ and the exact solution

$$u(x,y) = \sin(2\pi x)\sin(2\pi y)(x^3 - y^4 + x^2 y^2). \qquad (3.59)$$

We construct 5 grid levels and use Gauss-Seidel smoother. The number of Gauss-Seidel pre-smoothing and post-smoothing steps is 2. We stop the iter-

Table 3.3: Convergence results for the Poisson problem, Error

Grid	$\|u - u_h\|_0$	order	$|u - u_h|_1$	order
$2^4 \times 2^4$	4.2951E-03	-	3.9914E-01	-
$2^5 \times 2^5$	1.0682E-03	2.01	2.0028E-01	0.99
$2^6 \times 2^6$	2.6670E-04	2.00	1.0023E-01	1.00
$2^7 \times 2^7$	6.6653E-05	2.00	5.0126E-02	1.00
$2^8 \times 2^8$	1.6662E-05	2.00	2.5064E-02	1.00
$2^9 \times 2^9$	4.1654E-06	2.00	1.2532E-02	1.00

Table 3.4: Convergence results for the Poisson problem, # of iterations

Grid	No preconditioning	MILU0	AMG
$2^4 \times 2^4$	32	14	5
$2^5 \times 2^5$	67	21	5
$2^6 \times 2^6$	135	32	6
$2^7 \times 2^7$	272	48	6
$2^8 \times 2^8$	549	70	6
$2^9 \times 2^9$	1110	102	6

ation process when

$$\frac{\|\mathbf{r}_k\|_2}{\|\mathbf{f}\|_2} < 10^{-8} \qquad (3.60)$$

where $\mathbf{r}_k = \mathbf{f} - A\mathbf{x}_k$.

Optimal order convergence is observed Table 3.3. Table 3.4 shows that the AMG preconditioner gives a grid independent convergence for the Poisson problem.

Table 3.5: Convergence results for the Stokes problem

Grid	$\|u - u_h\|_0$	order	$|u - u_h|_1$	order	$\|p - p_h\|_0$	order
$2^4 \times 2^4$	1.0724E-04	-	8.8719E-03	-	2.9449E-02	-
$2^5 \times 2^5$	2.6795E-05	2.00	4.4498E-03	1.00	1.4730E-02	1.00
$2^6 \times 2^6$	6.6975E-06	2.00	2.2266E-03	1.00	7.3655E-03	1.00
$2^7 \times 2^7$	1.6743E-06	2.00	1.1135E-03	1.00	3.6828E-03	1.00
$2^8 \times 2^8$	4.1857E-07	2.00	5.5679E-04	1.00	1.8414E-03	1.00
$2^9 \times 2^9$	1.0466E-07	2.00	2.7840E-04	1.00	9.2071E-04	1.00

3.3.2 The stationary Stokes problem

The second test is carried out for determining the performance of the block preconditioner for the Stoke problem.

$$-\nu \triangle \mathbf{u} + \nabla p = \mathbf{f}, \text{in } \Omega$$
$$\nabla \cdot u = 0, \text{in } \Omega \quad (3.61)$$
$$\mathbf{u} = \mathbf{0}, \text{on } \partial \Omega$$

where $\Omega = [0,1]^2$ and the exact solution is

$$u(x, y) = \begin{pmatrix} -2x^2(x-1)^2 y(y-1)(2y-1) \\ 2y^2(y-1)^2 x(x-1)(2x-1) \end{pmatrix}, \quad (3.62)$$

$$p = x^2 + y^2 - \frac{2}{3} \quad (3.63)$$

and $\nu = 1$. Table 3.5 shows the convergence results for (3.61). Optimal order convergence is observed. Table 3.6 shows that inexact Uzawa method is efficient iterative solver for the Stokes problem.

Table 3.6: # of MINRES and inexact Uzawa iteration for the Stokes problem. In brackets is the number of seconds of CPU time.

Grid	MILU0-MINRERS	AMG-MINRES	inexact Uzawa
$2^4 \times 2^4$	53(0.0021)	31(0.0029)	5(0.0015)
$2^5 \times 2^5$	82(0.0142)	32(0.0145)	6(0.0082)
$2^6 \times 2^6$	119(0.0873)	35(0.0651)	6(0.0370)
$2^7 \times 2^7$	184(0.6836)	38(0.3280)	6(0.1841)
$2^8 \times 2^8$	277(3.8658)	40(1.3491)	7(0.8288)
$2^9 \times 2^9$	418(24.418)	43(6.3345)	7(3.7117)

Chapter 4

Numerical simulation of lid driven cavity flow

In this chapter, we discuss how to implement the stable P_1^{NC}-P_0 element for the lid driven incompressible viscous flow in a square cavity. We compute the steady state solutions of lid driven cavity flow by using conforming, Q_2-Q_1 and nonconforming, the stable P_1^{NC}-P_0 finite element and compare our results with those in published literature to validate the our implementation method.

4.1 Lid driven square cavity flow problem

The lid driven cavity problem is a very well known benchmark problem for two dimensional steady incompressible Navier-Stokes equations. Numerous numerical solutions can be found for this problem.

The lid driven square cavity flow problem is defined as follows:

$$
\begin{cases}
\dfrac{\partial \mathbf{u}}{\partial t} - \nu \triangle \mathbf{u} + (\mathbf{u} \cdot \nabla)\mathbf{u} + \nabla p = \mathbf{0}, \text{ in } \Omega \times (0,T), \\[2mm]
\nabla \cdot \mathbf{u} = 0, \text{ in } \Omega \times (0,T), \\[2mm]
\mathbf{u} = \mathbf{u}_0, \ t = 0, \\[2mm]
\mathbf{u} = \mathbf{g} \text{ on } \partial\Omega \times (0,T),
\end{cases}
\tag{4.1}
$$

with $\Omega = (0,1) \times (0,1)$ and $T \in (0, \infty]$. The Dirichlet boundary condition is defined as

$$
\mathbf{g}(x,y,t) =
\begin{cases}
(1,0), & \text{if } 0 < x < 1 \ \text{ and } \ y = 1 \\[2mm]
\mathbf{0}, & \text{elsewhere on } \partial\Omega
\end{cases}
, \ \forall t > 0.
\tag{4.2}
$$

$\mathbf{g}$ is discontinuous at top two corners $(0,1)$ and $(1,1)$. The presence of these singularities where velocity is discontinuous makes difficult to implement numerical methods. There are several ways to overcome corner singularities.

This difficulty has been overcome by regularizing boundary conditions on the upper lid. $\mathbf{g}$ is replaced by a function that vanishes at the corners where the lid and stationary walls meet. For example, Glowinski [23] solved the lid driven cavity problem by using the following boundary condition on the top of the cavity,

$$
f_a(x) =
\begin{cases}
\sin\left(\dfrac{\pi x}{2a}\right), & \text{if } 0 \le x < a \\[3mm]
1, & \text{if } a \le x \le 1 - a . \\[3mm]
\sin\left(\dfrac{\pi(1 - x)}{2a}\right), & \text{if } 1 - a < x \le 1
\end{cases}
\tag{4.3}
$$

Shen [44] used the boundary condition for the regularized driven cavity flow, $(16x^2(1 - x^2), 0)$ on the upper lid.

40

Barragy and Carey [5] used a p-type finite element formulation combined with a strongly graded and refined element mesh. They computed the numerical solutions on 256×256. They used weighted integral of velocity at corner singularities.

The lid driven cavity problem can be solved by using the Chebyshev collocation method [7]. This method is to subtract off the leading part of the known asymptotic form of the Navier-Stokes singularities.

Sahin and Owens [42] handled the corner singularities by introducing leaks over the height of the upper corner finite volumes.

Different numerical solutions of cavity flow yield about the same results for $Re \leq 1000$. However, they start to deviate from each other for large Reynolds number [19]. The published numerical results in the literature are obtained by using different numerical methods, the numbers of grids, and boundary conditions. These factors can affect numerical results of the lid driven cavity problem, comparing our numerical results with those in the literature in not enough to estimate the accuracy of the numerical results. We will compute numerical solutions of the lid driven cavity problem with and without modification of the problem. These numerical solutions are different from each other. Another test for the measurement of accuracy of the numerical solution is needed.

4.2   Indicators for accuracy

We use three indicators to check the accuracy of numerical solutions.

Incompressible condition   Since we solve the lid driven cavity problem by using the incompressible condition, numerical solution $\mathbf{u}_h$ should satisfy

$$\nabla \cdot \mathbf{u}_h = 0. \tag{4.4}$$

It is possible to check the incompressible condition by computing

$$\int_\Omega \nabla \cdot \mathbf{u}_h. \tag{4.5}$$

Let $\mathcal{T}_h$ be a partition of Ω into disjoint squares Q_j, $j = 1, \ldots, N^2$. Since $\nabla \cdot \mathbf{u} = 0$ for all $\mathbf{x} \in \Omega$,

$$\max_j \left| \int_{Q_j} \nabla \cdot \mathbf{u}_h \right| \tag{4.6}$$

is also a good indicator to check the accuracy. (4.5) and (4.6) of the numerical solution $\mathbf{u}_h$ should be close to zero.

Compatibility condition for stream function ψ   Let $\mathbf{u} = (u, v)$. Vorticity ω is defined as

$$\omega = \frac{\partial v}{\partial x} - \frac{\partial u}{\partial y}, \tag{4.7}$$

and the velocity components have to be

$$u = \frac{\partial \psi}{\partial y}, \ v = -\frac{\partial \psi}{\partial x} \tag{4.8}$$

in relation to the stream function ψ. Then, we have

$$\begin{aligned} -\triangle \psi &= \omega \text{ in } \Omega, \\ \frac{\partial \psi}{\partial n} &= g \text{ on } \Gamma (= \partial \Omega) \end{aligned} \tag{4.9}$$

with

$$\frac{\partial \psi}{\partial y} = 0, \text{ for } y = 0,$$

$$\frac{\partial \psi}{\partial y} = g, \text{ for } y = 1,$$

$$\frac{\partial \psi}{\partial x} = 0, \text{ for } x = 0, \quad \quad (4.10)$$

$$\frac{\partial \psi}{\partial x} = 0, \text{ for } x = 1$$

Compatibility condition gives

$$\int_\Omega \omega \, d\Omega = - \int_{\partial \Omega} g \, d\Gamma. \quad \quad (4.11)$$

Since g is known and we can compute $\int_\Omega \omega$ by using the numerical solution $\mathbf{u}_h$, we can compare two values to check the accuracy of the numerical solutions.

Volumetric flow rate   Aydin and Fenner [2] suggested a measurement of the accuracy of numerical solutions. They computed the net volumetric flow rate, Q, passing through a vertical line and horizontal line to check the continuity of the fluid. Let $Q_{u,c}$ and $Q_{v,c}$ be the volumetric flow rate passing through a vertical line, $x = c$ and horizontal line, $y = c$, respectively. The volumetric flow rate values, $Q_{u,c}$ and $Q_{v,c}$ can be computed by

$$Q_{u,c} = \left| \int_0^1 u(c, y) \, dy \right|, \quad \quad (4.12)$$

$$Q_{v,c} = \left| \int_0^1 v(x, c) \, dx \right|. \quad \quad (4.13)$$

4.3   Implementation of the stable P_1^{NC}-P_0 element

Since nonconforming finite element methods can avoid vertex degrees of freedom, the boundary values at top left and right corner are not required.

Thus, we can solve the lid driven cavity problem without modification of the boundary condition.

Let $\Omega = [0,1] \times [0,1]$ and $\mathcal{T}_h$ be a partition of Ω into disjoint squares Q_j, $j = 1, \ldots, N^2$ with size $h \times h$, $h = 1/N$. Let N_Q be the number of squares in $\mathcal{T}_h$, $N_Q = N^2$. The barycenter of $Q_{(k-1)N+j}$ is $(jh - h/2, kh - h/2)$, $j, k = 1, \ldots, N$. Let N_v^i be the number of interior vertices in $\mathcal{T}_h$. Then, $N_v^i = (N-1)^2$. There are $(N+1)^2$ nodes on the Ω. Let $c_{j,k}$ be an node located at $(x, y) = ((j-1)h, (k-1)h)$ for $j, k = 1, \ldots, N+1$.

The approximate solution $\mathbf{u}_h$ in P_1^{NC} is represented by

$$\mathbf{u}_h = \sum_{j=1}^{N_v^i} \xi_j \begin{pmatrix} \phi_j \\ 0 \end{pmatrix} + \sum_{j=1}^{N_v^i} \eta_j \begin{pmatrix} 0 \\ \phi_j \end{pmatrix} + \sum_{j=1}^{N_\partial} \alpha_j \begin{pmatrix} \phi_j \\ 0 \end{pmatrix} + \sum_{j=1}^{N_\partial} \beta_j \begin{pmatrix} 0 \\ \phi_j \end{pmatrix} \qquad (4.14)$$

where ϕ_j is the global basis functions for P_1-nonconforming quadrilateral finite element, $N_\partial = (N+1)^2 - N_v^i$, and $\alpha, \beta, \xi, \eta \in \mathbb{R}$. We are using the boundary condition (4.2), the approximate solution $\mathbf{u}_h$ can be written as

$$\mathbf{u}_h = \sum_{j=1}^{N_v} \xi_j \begin{pmatrix} \phi_j \\ 0 \end{pmatrix} + \sum_{j=1}^{N_v} \eta_j \begin{pmatrix} 0 \\ \phi_j \end{pmatrix} + \sum_{j=1}^{N-1} 0.5 \begin{pmatrix} \phi_{j,T} \\ 0 \end{pmatrix} \qquad (4.15)$$

where $\phi_{j,T}$ is the global basis functions for P_1-nonconforming quadrilateral finite element located at $c_{j+1,N+1}$. But

$$\sum_{j=1}^{N-1} 0.5 \begin{pmatrix} \phi_{j,T} \\ 0 \end{pmatrix} \qquad (4.16)$$

is not sufficient approximation of the boundary condition on the top of the cavity. We can have a sufficient approximation of the the boundary condition on the top of the cavity by introducing DSSY nonconforming finite element on the top left and right corner elements. This can be achieved as follows:

Replacing nonconforming P_1 by DSSY nonconforming finite element on the top left and right corner elements. DSSY in reference element, have the form

$$
\begin{aligned}
\widehat{\phi}_{1,\text{DSSY}} &= \frac{1}{4} + \frac{1}{2}x - \frac{3}{8}(\theta(x) - \theta(y)), \\
\widehat{\phi}_{2,\text{DSSY}} &= \frac{1}{4} + \frac{1}{2}y + \frac{3}{8}(\theta(x) - \theta(y)), \\
\widehat{\phi}_{3,\text{DSSY}} &= \frac{1}{4} - \frac{1}{2}x - \frac{3}{8}(\theta(x) - \theta(y)), \\
\widehat{\phi}_{4,\text{DSSY}} &= \frac{1}{4} - \frac{1}{2}y + \frac{3}{8}(\theta(x) - \theta(y)),
\end{aligned}
\tag{4.17}
$$

where $\theta(x) = x^2 - \frac{5}{3}x^4$. Since the continuity across the inter-element interfaces, the top left element is approximated by

$$
\widehat{\phi}_{1,\text{DSSY}} + \widehat{\phi}_{4,\text{DSSY}} = \frac{1}{2} + \frac{x}{2} - \frac{y}{2},
\tag{4.18}
$$

and the top right element is approximated by

$$
\widehat{\phi}_{3,\text{DSSY}} + \widehat{\phi}_{4,\text{DSSY}} = \frac{1}{2} - \frac{x}{2} - \frac{y}{2}.
\tag{4.19}
$$

(4.18) and (4.19) are local basis functions of nonconforming P_1 on the top left and right corner elements. Replacement nonconforming P_1 by DSSY noncon-forming finite element on the top left and right corner element does not affect coefficients of (3.7), (3.11), and (3.14). Let $\widetilde{\phi}_{j,Q}$ be the DSSY nonconforming basis functions for element Q. Then, we can obtain the approximate solution, $\mathbf{u}_h$ has the form

$$
\mathbf{u}_h = \sum_{j=1}^{N_v} \xi_j \begin{pmatrix} \phi_j \\ 0 \end{pmatrix} + \sum_{j=1}^{N_v} \eta_j \begin{pmatrix} 0 \\ \phi_j \end{pmatrix} + \sum_{j=1}^{N-1} 0.5 \begin{pmatrix} \phi_{j,T} \\ 0 \end{pmatrix} + 0.5 \begin{pmatrix} \widetilde{\phi}_{2,TL} + \widetilde{\phi}_{2,TR} \\ 0 \end{pmatrix}
\tag{4.20}
$$

where TL and TR represent the top left and right corner elements for the cavity.

4.4 Numerical simulation

We have computed the steady state solutions of lid driven cavity flow from $Re = 100$ to $Re = 5000$ by using the Piacard correction. The Picard iteration is terminated when

$$\left\| \begin{pmatrix} \mathbf{f} - \nu A \mathbf{u}^{(k)} - N\mathbf{u}^{(k)} - B^T \mathbf{p}^{(k)} \\ \mathbf{g} - B\mathbf{u}^{(k)} \end{pmatrix} \right\| \leq 10^{-10} \begin{pmatrix} \mathbf{f} \\ \mathbf{g} \end{pmatrix}. \tag{4.21}$$

We solved the regularized driven cavity problem by using the stable P_1^{NC}-P_0 finite element and $Q_2 - Q_1$ conforming finite element. The approximate solution $\mathbf{u}_h$ has the form

$$\mathbf{u}_h = \sum_{j=1}^{N_v} \xi_j \begin{pmatrix} \phi_j \\ 0 \end{pmatrix} + \sum_{j=1}^{N_v} \eta_j \begin{pmatrix} 0 \\ \phi_j \end{pmatrix} + \sum_{j=1}^{N-1} \gamma_j \begin{pmatrix} \phi_{j,T} \\ 0 \end{pmatrix} \tag{4.22}$$

for the stable P_1^{NC}-P_0 finite element. We used (4.3) as the boundary condition for the top of the cavity and a parameter $a = 1/32$ for (4.3).

We computed numerical solutions for the unregularized driven cavity problem by using the stable P_1^{NC}-P_0 finite element. The approximate solution $\mathbf{u}_h$ has the form

$$\mathbf{u}_h = \sum_{j=1}^{N_v} \xi_j \begin{pmatrix} \phi_j \\ 0 \end{pmatrix} + \sum_{j=1}^{N_v} \eta_j \begin{pmatrix} 0 \\ \phi_j \end{pmatrix} + \sum_{j=1}^{N-1} 0.5 \begin{pmatrix} \phi_{j,T} \\ 0 \end{pmatrix} + 0.5 \begin{pmatrix} \widetilde{\phi}_{2,TL} + \widetilde{\phi}_{2,TR} \\ 0 \end{pmatrix} \tag{4.23}$$

for the stable P_1^{NC}-P_0 finite element when unregularized boundary condition is used. We also computed numerical solutions by using Q_2-Q_1 conforming finite element for the lid driven cavity problem with boundary condition which satisfies

$$- \int_{\partial \Omega} g \, d\Gamma = -1. \tag{4.24}$$

46

It is required to evaluate values at the top left and right corner points on Ω for Q_2-Q_1 conforming finite element. In [18], there are two boundary conditions for the cavity problem which satisfy (4.24). A leaky cavity boundary condition is defined as

$$
\mathbf{g} = \begin{cases} (1,0), & \text{if } 0 \leq x \leq 1 \;\; \text{and} \;\; y = 1 \\ \mathbf{0}, & \text{elsewhere on } \partial\Omega \end{cases} \tag{4.25}
$$

and a watertight cavity boundary condition is defined as

$$
\mathbf{g} = \begin{cases} (1,0), & \text{if } 0 < x < 1 \;\; \text{and} \;\; y = 1 \\ \mathbf{0}, & \text{elsewhere on } \partial\Omega \end{cases}. \tag{4.26}
$$

$\mathbf{g}(0,1) = (0,0)$ and $\mathbf{g}(1,1) = (0,0)$ for a watertight cavity boundary condition. We computed the numerical solutions of lid driven cavity problem with (4.25) and (4.26) by using Q_2-Q_1 conforming finite element.

We developed our own FORTRAN and MATLAB codes for the lid driven cavity problem by using the stable P_1^{NC}-P_0 finite element. And we used IFISS [36] to compute the numerical solutions of the lid driven cavity problem by using Q_2-Q_1 conforming finite element.

For an assessment of the accuracy of the numerical results, (4.5), (4.6), and (4.11) for the stable P_1^{NC}-P_0 and Q_2-Q_1 are computed and compared with the exact values of incompressible and compatibility conditions. Since $\nabla \cdot \mathbf{u} = 0$, the exact values of (4.5) and (4.6) are zero. For unregularized, leaky, and watertight boundary conditions,

$$
\int_\Omega \omega \, d\Omega = -\int_{\partial\Omega} g \, d\Gamma = -1. \tag{4.27}
$$

Table 4.1: Incompressible and compatibility conditions for the stable P_1^{NC}-P_0.

	Grid	(4.5)	(4.6)	(4.11)	Regularization
Re = 100					
P_1^{NC}-P_0	128×128	6.1427E-18	4.7684E-07	-1.000000	no
P_1^{NC}-P_0	128×128	1.3565E-17	9.4849E-08	-0.976776	(4.3)
P_1^{NC}-P_0	256×256	2.5218E-18	5.9605E-08	-1.000000	no
P_1^{NC}-P_0	256×256	1.1686E-17	5.8705E-09	-0.977161	(4.3)
Re = 400					
P_1^{NC}-P_0	128×128	2.5167E-17	4.7684E-07	-1.000000	no
P_1^{NC}-P_0	128×128	2.5129E-17	9.4849E-08	-0.976776	(4.3)
P_1^{NC}-P_0	256×256	5.1101E-18	5.9605E-08	-1.000000	no
P_1^{NC}-P_0	256×256	4.8115E-17	5.8705E-09	-0.977161	(4.3)
Re = 1000					
P_1^{NC}-P_0	128×128	5.2660E-18	4.7684E-07	-1.000000	no
P_1^{NC}-P_0	128×128	7.5021E-18	9.4849E-08	-0.976776	(4.3)
P_1^{NC}-P_0	256×256	6.5539E-20	5.9605E-08	-1.000000	no
P_1^{NC}-P_0	256×256	1.7428E-17	5.8705E-09	-0.977161	(4.3)
Re = 2500					
P_1^{NC}-P_0	256×256	2.1456E-17	5.9605E-08	-1.000000	no
P_1^{NC}-P_0	256×256	1.9819E-17	5.8705E-09	-0.977161	(4.3)
Re = 3200					
P_1^{NC}-P_0	256×256	2.1456E-17	5.9605E-08	-1.000000	no
P_1^{NC}-P_0	256×256	2.7092E-17	5.8705E-09	-0.977161	(4.3)
Re = 5200					
P_1^{NC}-P_0	256×256	4.7180E-18	5.9605E-08	-1.000000	no
P_1^{NC}-P_0	256×256	1.7666E-20	5.8705E-09	-0.977161	(4.3)

If we use (4.3),

$$\int_\Omega \omega \, d\Omega = - \int_{\partial\Omega} g \, d\Gamma = - \left(\frac{1}{8\pi} + \frac{15}{16} \right) \approx -0.97728884. \qquad (4.28)$$

As seen in Table 4.1 and Table 4.2, numerical solutions of the lid driven cavity problem by using both the stable P_1^{NC}-P_0 and Q_2-Q_1 seem to satisfy the incompressible condition well. (4.5) of both the stable P_1^{NC}-P_0 and Q_2-Q_1 are very small. When viewing Table 4.1, one can see that the values of (4.5) computed by using the stable P_1^{NC}-P_0 finite element are almost zero.

Let $\mathcal{T}_h$ be treated as a checkerboard with red and black squares. Let $R = \{Q_{R_1}, \ldots, Q_{R_{N_Q/2}}\}$ and $B = \{Q_{B_1}, \ldots, Q_{B_{N_Q/2}}\}$ be the set of red and black

Table 4.2: Incompressible and compatibility conditions for Q_2-Q_1.

	Grid	(4.5)	(4.6)	(4.11)	Regularization
Re = 100					
Q_2-Q_1	128×128	3.1913E-16	3.3407E-04	-1.000000	leaky
Q_2-Q_1	128×128	3.0737E-16	6.1596E-04	-0.997396	watertight
Q_2-Q_1	128×128	3.4624E-16	8.0701E-05	-0.977289	(4.3)
Re = 400					
Q_2-Q_1	128×128	3.8272E-16	3.9730E-04	-1.000000	leaky
Q_2-Q_1	128×128	3.9996E-16	6.6730E-04	-0.997396	watertight
Q_2-Q_1	128×128	3.7101E-16	8.7626E-05	-0.977289	(4.3)
Re = 1000					
Q_2-Q_1	128×128	3.8955E-16	5.0746E-04	-1.000000	leaky
Q_2-Q_1	128×128	4.0018E-16	7.2274E-04	-0.997396	watertight
Q_2-Q_1	128×128	4.0690E-16	1.1443E-04	-0.977289	(4.3)
Re = 2500					
Q_2-Q_1	128×128	3.3339E-16	5.9441E-04	-1.000000	leaky
Q_2-Q_1	128×128	3.6711E-16	1.1836E-03	-0.997396	watertight
Q_2-Q_1	128×128	3.0629E-16	3.1994E-04	-0.977289	(4.3)
Re = 3200					
Q_2-Q_1	128×128	2.7409E-16	6.0657E-04	-1.000000	leaky
Q_2-Q_1	128×128	3.1724E-16	1.3685E-03	-0.997396	watertight
Q_2-Q_1	128×128	3.7416E-16	2.6122E-04	-0.977289	(4.3)
Re = 5000					
Q_2-Q_1	128×128	2.0491E-16	6.7909E-04	-1.000000	leaky
Q_2-Q_1	128×128	2.0838E-16	1.6240E-03	-0.997396	watertight
Q_2-Q_1	128×128	2.4286E-16	4.2536E-04	-0.977289	(4.3)

squares such that $R \cup B = \mathcal{T}_h$. Set $Q_{R_1} = Q_1$ and $Q_{B_1} = Q_2$. We can observe that

$$\left| \int_{Q_j} \nabla \cdot \mathbf{u}_h \right| \tag{4.29}$$

are the same values for $j = 1, \ldots, N_Q$ and

$$\int_{Q_{R_j}} \nabla \cdot \mathbf{u}_h = \alpha, \ j = 1, \ldots, N_Q/2,$$
$$\int_{Q_{B_j}} \nabla \cdot \mathbf{u}_h = \beta, \ j = 1, \ldots, N_Q/2, \tag{4.30}$$

$\alpha + \beta = 0$.

Theorem 4. *Let* $\mathbf{u}_h$ *be* (4.22) *or* (4.23). *And*

$$\int_{\Omega} q_h (\nabla \cdot \mathbf{u}_h) = 0, \ \forall q_h \in P_{cf}^h. \tag{4.31}$$

Then

$$\int_{\Omega} \nabla \cdot \mathbf{u}_h = 0. \tag{4.32}$$

Proof. Since

$$\int_{\Omega} \frac{\partial}{\partial x} \tilde{\phi}_{2,TL} = \int_{\Omega} \frac{\partial}{\partial x} \tilde{\phi}_{2,TR} = 0, \tag{4.33}$$

it is enough to consider (4.22) only.

Let $N = 2^j$, $j = 1, \ldots$, $h = 1/N$, and $N_Q = N^2$. The basis function of P_{cf}^h,

ψ_k has the form

$$\psi_k(\mathbf{x}) = \begin{cases} 1, & \mathbf{x} \in Q_{R_k} \\ -1, & \mathbf{x} \in Q_{R_{k+1}} \quad \text{for } k = 1, \ldots, \frac{N_Q}{2} - 1, \\ 0, & \text{otherwise} \end{cases}$$

(4.34)

$$\psi_{N_Q/2-1+k}(\mathbf{x}) = \begin{cases} 1, & \mathbf{x} \in Q_{B_k} \\ -1, & \mathbf{x} \in Q_{B_{k+1}} \quad \text{for } k = 1, \ldots, \frac{N_Q}{2} - 1. \\ 0, & \text{otherwise} \end{cases}$$

where $R = \{Q_{R_1}, \ldots, Q_{R_{N_Q/2}}\}$ and $B = \{Q_{B_1}, \ldots, Q_{B_{N_Q/2}}\}$ be the set of red and black squares such that $R \cup B = \mathcal{T}_h$. Since ϕ_j is linear, $\nabla \cdot \mathbf{u}_h$ is constant. Since $\int_\Omega q_h(\nabla \cdot \mathbf{u}_h) \, dx = 0$ for all $q_h \in P_{cf}^h$,

$$\int_{Q_{R_j}} \nabla \cdot \mathbf{u}_h = \alpha \text{ and } \int_{Q_{B_j}} \nabla \cdot \mathbf{u}_h = \beta \text{ for } j = 1, \ldots, \frac{N_Q}{2}.$$

(4.35)

By using

$$\nabla \phi_{(k-1)(N-1)+j} = \begin{cases} \left(\frac{1}{h}, \frac{1}{h}\right), & \text{on } Q_{(k-1)N+j} \\ \left(-\frac{1}{h}, \frac{1}{h}\right), & \text{on } Q_{(k-1)N+j+1} \\ \left(-\frac{1}{h}, -\frac{1}{h}\right), & \text{on } Q_{kN+j+1} \\ \left(\frac{1}{h}, -\frac{1}{h}\right), & \text{on } Q_{kN+j} \end{cases}$$

(4.36)

for $j, k = 1, \ldots, N - 1$, we can obtain

$$
\begin{aligned}
\sum_{l=1}^{N_Q/2} \int_{Q_{R_l}} \nabla \cdot \mathbf{u}_h &= h \sum_{k=1}^{N-1} (-1)^k \gamma_k = \frac{N_Q}{2} \alpha, \\
\sum_{l=1}^{N_Q/2} \int_{Q_{B_l}} \nabla \cdot \mathbf{u}_h &= h \sum_{k=1}^{N-1} (-1)^{k+1} \gamma_k = \frac{N_Q}{2} \beta.
\end{aligned}
\tag{4.37}
$$

Thus, $\alpha + \beta = 0$. We can obtain

$$
\int_{\Omega} \nabla \cdot \mathbf{u}_h = \frac{N_Q}{2} (\alpha + \beta) = 0.
\tag{4.38}
$$

$\square$

For P_1^{NC}-P_0 with unregularized boundary condition on 128×128 grid,

$$
\alpha = -\beta = 2 \times \frac{1}{128} \times \frac{1}{128^2} \times \sum_{k=1}^{N-1} (-1)^k \gamma_k = -4.7684\text{E-}07
\tag{4.39}
$$

and on 256×256 grid,

$$
\alpha = -\beta = 2 \times \frac{1}{256} \times \frac{1}{256^2} \times \sum_{k=1}^{N-1} (-1)^k \gamma_k = -5.9605\text{E-}08.
\tag{4.40}
$$

For P_1^{NC}-P_0 with (4.3) on 128×128 grid,

$$
\alpha = -\beta = 2 \times \frac{1}{128} \times \frac{1}{128^2} \times \sum_{k=1}^{N-1} (-1)^k \gamma_k = -9.4849\text{E-}08
\tag{4.41}
$$

and on 256×256 grid,

$$
\alpha = -\beta = 2 \times \frac{1}{256} \times \frac{1}{256^2} \times \sum_{k=1}^{N-1} (-1)^k \gamma_k = -5.8705\text{E-}09.
\tag{4.42}
$$

These values are matched with the results in Table 4.1. In terms of (4.6), numerical results for the stable P_1^{NC}-P_0 finite element are more accurate than numerical results of Q_2-Q_1. Moreover, values of (4.6) for the stable P_1^{NC}-P_0 finite element are independent on Reynolds number. And (4.6) is getting close to zero as N increases by Theorem 4, when the stable P_1^{NC}-P_0 finite element is used. In contrast, Table 4.2 shows an increasing tendency of values of (4.6) for Q_2-Q_1 as the increase of Reynolds number.

When regularize boundary condition (4.3) is used, (4.11) for Q_2-Q_1 is closer to the exact value than (4.11) for the stable P_1^{NC}-P_0. Numerical results of the stable P_1^{NC}-P_0 with the unregularized boundary condition and Q_2-Q_1 with the leaky cavity boundary condition, satisfy the compatibility condition precisely.

The volumetric flow rate values for the the stable P_1^{NC}-P_0 in Table 4.3 and Table 4.4 are close to zero. Q_{u,x_c} and Q_{v,y_c} for Q_2-Q_1 are very large compared with $Q_{u,x_c-h/2}$, $Q_{u,x_c+h/2}$, $Q_{v,y_c-h/2}$, and $Q_{v,y_c+h/2}$ for the stable P_1^{NC}-P_0.

These three indicators for the accuracy show that our numerical solutions are accurate. Judged by the incompressible and compatibility conditions, the numerical solutions computed by using the stable P_1^{NC}-P_0 are more accurate than those obtained by using Q_2-Q_1 conforming finite element.

In Table 4.6–Table 4.10, we present the location of the center of the primary vortex, the stream function ψ, and vorticity ω at vortex center. These data are provided for $100 \leq \text{Re} \leq 5000$ and available comparison data from the literatures are also given. We evaluate values of the stream function ψ and vorticity ω at the center of meshes when the stable P_1^{NC}-P_0 is nonconforming finite element is used. Our numerical solutions computed by using both the stable P_1^{NC}-P_0 and Q_2-Q_1 exhibit a good agreement with the literature data except in the case of the numerical solutions computed by using Q_2-Q_1 with leaky cavity boundary condition. ψ and ω for the stable P_1^{NC}-P_0 with

Table 4.3: Volumetric flow rates through vertical lines, (x_c, y_c): the geometric center of the cavity.

	Grid	$Q_{u,x_c-h/2}$	$Q_{u,x_c+h/2}$	Regularization
Re = 100				
P_1^{NC}-P_0	128×128	3.1225E-17	8.8471E-17	no
P_1^{NC}-P_0	128×128	5.8113E-17	7.4593E-17	(4.3)
P_1^{NC}-P_0	256×256	1.2120E-13	1.1341E-13	no
P_1^{NC}-P_0	256×256	1.1432E-15	1.0881E-15	(4.3)
Re = 400				
P_1^{NC}-P_0	128×128	2.8883E-16	1.9863E-16	no
P_1^{NC}-P_0	128×128	3.1919E-16	1.6220E-16	(4.3)
P_1^{NC}-P_0	256×256	1.2214E-14	1.2363E-14	no
P_1^{NC}-P_0	256×256	9.9747E-18	6.2016E-17	(4.3)
Re = 1000				
P_1^{NC}-P_0	128×128	2.0903E-16	2.2551E-17	no
P_1^{NC}-P_0	128×128	3.1919E-16	1.6220E-16	(4.3)
P_1^{NC}-P_0	256×256	3.5432E-16	3.6559E-16	no
P_1^{NC}-P_0	256×256	3.3090E-16	1.6870E-16	(4.3)
Re = 2500				
P_1^{NC}-P_0	256×256	3.2504E-16	3.1507E-16	no
P_1^{NC}-P_0	256×256	1.3401E-16	2.7279E-16	(4.3)
Re = 3200				
P_1^{NC}-P_0	256×256	3.1485E-16	7.1167E-16	no
P_1^{NC}-P_0	256×256	1.7998E-16	4.1200E-17	(4.3)
Re = 5000				
P_1^{NC}-P_0	256×256	1.3661E-16	3.3133E-16	no
P_1^{NC}-P_0	256×256	7.7629E-17	1.3964E-16	(4.3)

Table 4.4: Volumetric flow rates through horizontal lines, (x_c, y_c): the geometric center of the cavity.

	Grid	$Q_{v,y_c-h/2}$	$Q_{v,y_c+h/2}$	Regularization
Re = 100				
P_1^{NC}-P_0	128×128	1.4250E-14	1.4504E-14	no
P_1^{NC}-P_0	128×128	7.0072E-15	7.2908E-15	(4.3)
P_1^{NC}-P_0	256×256	1.5536E-10	1.5424E-10	no
P_1^{NC}-P_0	256×256	5.0167E-14	5.0838E-14	(4.3)
Re = 400				
P_1^{NC}-P_0	128×128	1.8380E-14	1.8338E-14	no
P_1^{NC}-P_0	128×128	1.8687E-14	1.8968E-14	(4.3)
P_1^{NC}-P_0	256×256	5.2912E-12	5.3314E-12	no
P_1^{NC}-P_0	256×256	3.3504E-15	3.4528E-15	(4.3)
Re = 1000				
P_1^{NC}-P_0	128×128	2.2944E-14	2.2427E-14	no
P_1^{NC}-P_0	128×128	2.3881E-14	2.4729E-14	(4.3)
P_1^{NC}-P_0	256×256	5.9878E-14	5.8596E-14	no
P_1^{NC}-P_0	256×256	2.4952E-14	2.4661E-14	(4.3)
Re = 2500				
P_1^{NC}-P_0	256×256	1.2042E-13	1.2203E-13	no
P_1^{NC}-P_0	256×256	1.3188E-13	1.3211E-13	(4.3)
Re = 3200				
P_1^{NC}-P_0	256×256	3.3047E-14	3.5256E-14	no
P_1^{NC}-P_0	256×256	2.2349E-14	2.3200E-14	(4.3)
Re = 5000				
P_1^{NC}-P_0	256×256	4.4101E-14	4.5367E-14	no
P_1^{NC}-P_0	256×256	5.4802E-14	5.4890E-14	(4.3)

Table 4.5: Volumetric flow rates through horizontal lines, (x_c, y_c): the geometric center of the cavity.

	Grid	Q_{u,x_c}	Q_{v,y_c}	Regularization
Re = 100				
Q_2-Q_1	128×128	1.3114E-03	9.7804E-08	leaky
Q_2-Q_1	128×128	9.3009E-06	6.5662E-08	watertight
Q_2-Q_1	128×128	9.3013E-06	6.5937E-08	(4.3)
Re = 400				
Q_2-Q_1	128×128	1.3170E-03	1.1132E-06	leaky
Q_2-Q_1	128×128	1.4876E-05	1.2495E-06	watertight
Q_2-Q_1	128×128	1.4889E-05	1.2449E-06	(4.3)
Re = 1000				
Q_2-Q_1	128×128	1.3264E-03	2.5407E-06	leaky
Q_2-Q_1	128×128	2.4097E-05	2.8794E-06	watertight
Q_2-Q_1	128×128	2.4155E-05	2.8561E-06	(4.3)
Re = 2500				
Q_2-Q_1	128×128	1.3431E-03	4.8544E-06	leaky
Q_2-Q_1	128×128	4.0694E-05	5.7553E-06	watertight
Q_2-Q_1	128×128	4.0864E-05	5.6905E-06	(4.3)
Re = 3200				
Q_2-Q_1	128×128	1.3494E-03	5.8405E-06	leaky
Q_2-Q_1	128×128	4.6986E-05	7.0223E-06	watertight
Q_2-Q_1	128×128	4.7202E-05	6.9434E-06	(4.3)
Re = 5000				
Q_2-Q_1	128×128	1.3634E-03	8.2691E-06	leaky
Q_2-Q_1	128×128	6.1055E-05	1.0206E-05	watertight
Q_2-Q_1	128×128	6.1368E-05	1.0107E-05	(4.3)

Table 4.6: Properties of the primary vortex; minimum values of stream function (ψ), vorticity (ω), and location (x, y) for Re = 100.

	Grid	ψ	ω	(x, y)	Regularization
P_1^{NC}-P_0	128×128	-0.103559	3.15120	(0.6133,0.7383)	no
P_1^{NC}-P_0	128×128	-0.103560	3.15336	(0.6133,0.7383)	(4.3)
P_1^{NC}-P_0	256×256	-0.103531	3.16206	(0.6152,0.7363)	no
P_1^{NC}-P_0	256×256	-0.103531	3.16061	(0.6152,0.7363)	(4.3)
Q_2-Q_1	128×128	-0.102872	3.15485	(0.6172,0.7383)	leaky
Q_2-Q_1	128×128	-0.103519	3.18101	(0.6172,0.7383)	watertight
Q_2-Q_1	128×128	-0.103520	3.18085	(0.6172,0.7383)	(4.3)
[21]	129×129	-0.103423	3.16646	(0.6172,0.7344)	-
[23]	128×128	-0.103435	-	(0.6172,0.7344)	(4.3)
[26]	81×81	-0.103	-	(0.6188,0.7375)	-
[29]	256×256	-0.1030	-	(0.6196,0.7373)	[29]
[42]	257×257	-0.103471	3.1655	(0.6189,0.7400)	[42]

unregularized boundary condition are bigger than the others results. It might be due to unregularized boundary condition. We can see the similar situation that ψ and ω with watertight cavity boundary condition are bigger than ψ and ω with (4.3).

In Figure 4.1–Figure 4.6, we present the u-velocity profiles along the line $x = 0.5$ and the v-velocity profiles along the line $y = 0.5$ computed by using the stable P_1^{NC}-P_0 with unregularized boundary condition and Q_2-Q_1 with watertight boundary condition for Reynolds numbers ranging from 100 to 5000 and compared our results with those from [19] and [21]. The comparison shows good agreement for both the stable P_1^{NC}-P_0 and Q_2-Q_1. As seen from Figure 4.1 to Figure 4.6, as Reynold number increases the extreme values of u and v increase in magnitude. We can observe that near linearity of those profiles in the central core of the cavity in Figure 4.1–Figure 4.6. This is indicative of a large uniform vorticity region [24].

Table 4.7: Properties of the primary vortex; minimum values of stream function (ψ), vorticity (ω), and location (x, y) for Re = 400.

	Grid	ψ	ω	(x, y)	Regularization
P_1^{NC}-P_0	128×128	-0.114313	2.30535	(0.5508,0.6055)	no
P_1^{NC}-P_0	128×128	-0.114287	2.30683	(0.5508,0.6055)	(4.3)
P_1^{NC}-P_0	256×256	-0.114071	2.29821	(0.5527,0.6035)	no
P_1^{NC}-P_0	256×256	-0.114048	2.29904	(0.5527,0.6035)	(4.3)
Q_2-Q_1	128×128	-0.111900	2.26041	(0.5547,0.6055)	leaky
Q_2-Q_1	128×128	-0.113990	2.29476	(0.5547,0.6055)	watertight
Q_2-Q_1	128×128	-0.113969	2.29476	(0.5547,0.6055)	(4.3)
[21]	257×257	-0.113909	2.29469	(0.5547,0.6055)	-
[23]	128×128	-0.113909	-	(0.5547,0.6094)	(4.3)
[26]	81×81	-0.113	-	(0.5500,0.6125)	-
[29]	256×256	-0.1121	-	(0.5608,0.6078)	[29]
[42]	257×257	-0.113897	2.2950	(0.5536,0.6075)	[42]

Table 4.8: Properties of the primary vortex; minimum values of stream function (ψ), vorticity (ω), and location (x, y) for Re = 1000.

	Grid	ψ	ω	(x, y)	Regularization
P_1^{NC}-P_0	128×128	-0.119888	2.08605	(0.5273,0.5664)	no
P_1^{NC}-P_0	128×128	-0.119783	2.08584	(0.5273,0.5664)	(4.3)
P_1^{NC}-P_0	256×256	-0.119185	2.07215	(0.5293,0.5645)	no
P_1^{NC}-P_0	256×256	-0.119084	2.07146	(0.5293,0.5645)	(4.3)
Q_2-Q_1	128×128	-0.115376	2.00941	(0.5313,0.5664)	leaky
Q_2-Q_1	128×128	-0.118941	2.06779	(0.5313,0.5664)	watertight
Q_2-Q_1	128×128	-0.118846	2.06660	(0.5313,0.5664)	(4.3)
[6]	160×160	-0.118937	2.06775	-	[6]
[13]	1024×1024	-0.11892	2.0674	-	[13]
[19]	601×601	-0.118781	2.06553	(0.5300,0.5650)	-
[21]	257×257	-0.117929	2.04968	(0.5313,0.5625)	-
[23]	128×128	-0.119173	-	(0.5313,0.5625)	(4.3)
[26]	81×81	-0.117	-	(0.5250,0.5625)	-
[29]	256×256	-0.1178	-	(0.5333,0.5647)	[29]
[42]	257×257	-0.118800	2.0664	(0.5335,0.5639)	[42]

Table 4.9: Properties of the primary vortex; minimum values of stream function (ψ), vorticity (ω), and location (x, y) for Re = 2500.

	Grid	ψ	ω	(x, y)	Regularization
Re = 2500					
P_1^{NC}-P_0	256×256	-0.122157	1.98920	(0.5215,0.5449)	no
P_1^{NC}-P_0	256×256	-0.121894	1.98509	(0.5215,0.5449)	(4.3)
Q_2-Q_1	128×128	-0.115717	1.88476	(0.5195,0.5430)	leaky
Q_2-Q_1	128×128	-0.121492	1.97645	(0.5195,0.5430)	watertight
Q_2-Q_1	128×128	-0.121250	1.97314	(0.5195,0.5430)	(4.3)
[19]	601×601	-0.121035	1.96968	(0.5200,0.5433)	-

Table 4.10: Properties of the primary vortex; minimum values of stream function (ψ), vorticity (ω), and location (x, y) for Re = 3200.

	Grid	ψ	ω	(x, y)	Regularization
P_1^{NC}-P_0	256×256	-0.122726	1.97796	(0.5176,0.5410)	no
P_1^{NC}-P_0	256×256	-0.122407	1.97308	(0.5176,0.5410)	(4.3)
Q_2-Q_1	128×128	-0.115310	1.85833	(0.5195,0.5430)	leaky
Q_2-Q_1	128×128	-0.121860	1.96186	(0.5195,0.5391)	watertight
Q_2-Q_1	128×128	-0.121565	1.95776	(0.5195,0.5391)	(4.3)
[21]	257×257	-0.120377	1.98860	(0.5165,0.5469)	-
[23]	128×128	-0.121768	-	(0.5165,0.5352)	(4.3)
[26]	161×161	-0.122	-	(0.5125,0.5375)	-
[42]	257×257	-0.121628	1.9593	(0.5201,0.5376)	[42]

Table 4.11: Properties of the primary vortex; minimum values of stream function (ψ), vorticity (ω), and location (x, y) for Re = 5000.

	Grid	ψ	ω	(x, y)	Regularization
P_1^{NC}-P_0	256×256	-0.123698	1.96709	(0.5137,0.5371)	no
P_1^{NC}-P_0	256×256	-0.123270	1.96058	(0.5137,0.5371)	(4.3)
Q_2-Q_1	128×128	-0.114120	1.81321	(0.5156,0.5352)	leaky
Q_2-Q_1	128×128	-0.122368	1.94277	(0.5156,0.5352)	watertight
Q_2-Q_1	128×128	-0.121905	1.93620	(0.5156,0.5352)	(4.3)
[13]	1024×1024	-0.12200	1.9343	-	[13]
[19]	601×601	-0.121289	1.92660	(0.5150,0.5350)	-
[21]	257×257	-0.118966	1.86016	(0.5117,0.5352)	-
[23]	128×128	-0.121218	-	(0.5156,0.5352)	(4.3)
[26]	161×161	-0.122	-	(0.5125,0.5375)	-
[29]	256×256	-0.1214	-	(0.5176,0.5373)	[29]
[42]	257×257	-0.122050	1.9392	(0.5134,0.5376)	[42]

Figure 4.1: Profiles of u-velocity along the line $x = 0.5$ and v-velocity along $y = 0.5$ computed by using the stable P_1^{NC}-P_0 with unregularized boundary condition and Q_2-Q_1 with watertight boundary condition, Re $= 100$.
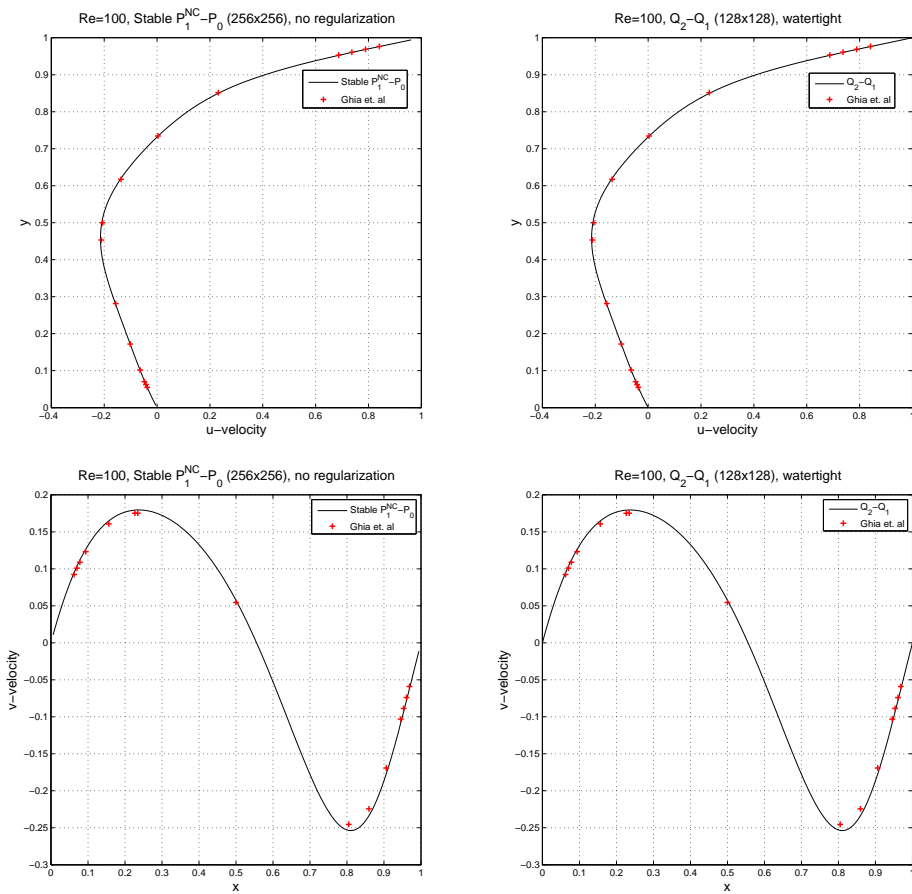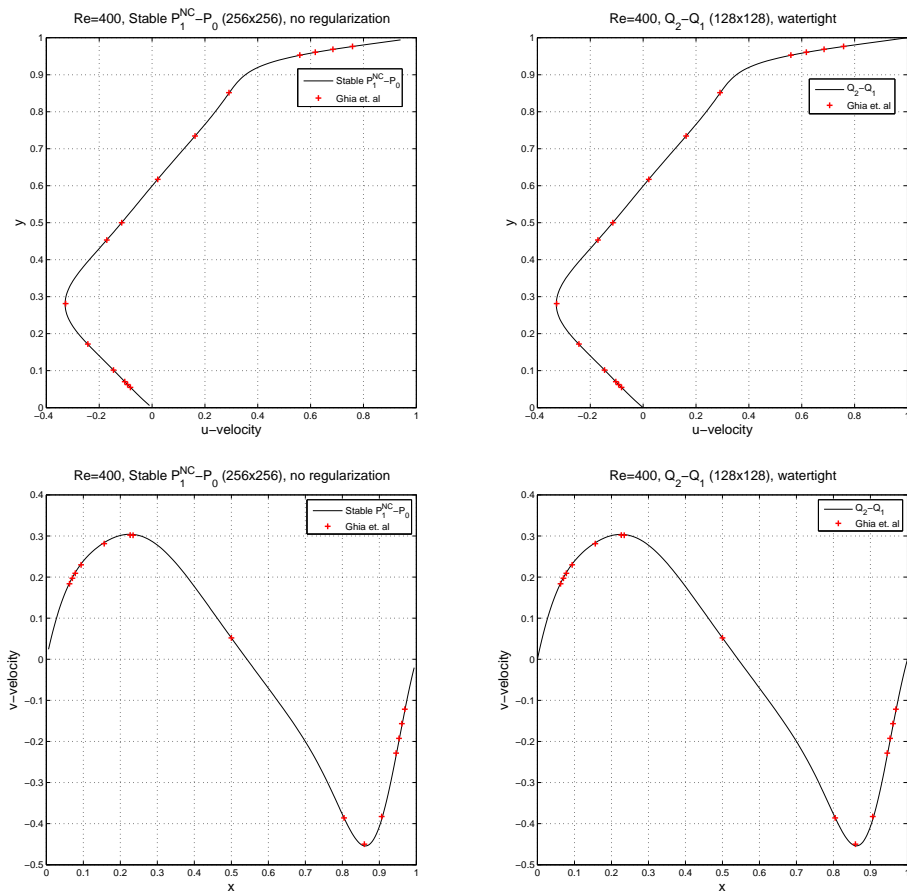
Figure 4.2: Profiles of u-velocity along the line $x = 0.5$ and v-velocity along $y = 0.5$ computed by using the stable P_1^{NC}-P_0 with unregularized boundary condition and Q_2-Q_1 with watertight boundary condition, Re = 400.

Figure 4.3: Profiles of u-velocity along the line $x = 0.5$ and v-velocity along $y = 0.5$ computed by using the stable P_1^{NC}-P_0 with unregularized boundary condition and Q_2-Q_1 with watertight boundary condition, Re = 1000.
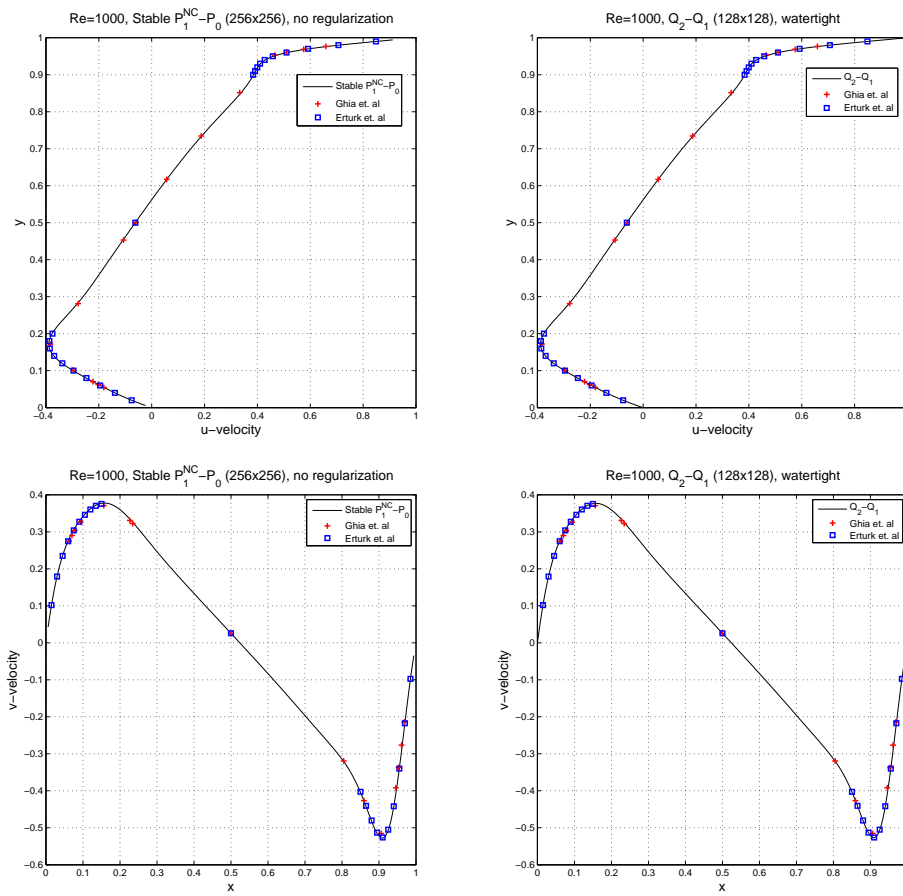
Figure 4.4: Profiles of u-velocity along the line $x = 0.5$ and v-velocity along $y = 0.5$ computed by using the stable P_1^{NC}-P_0 with unregularized boundary condition and Q_2-Q_1 with watertight boundary condition, Re $= 2500$.
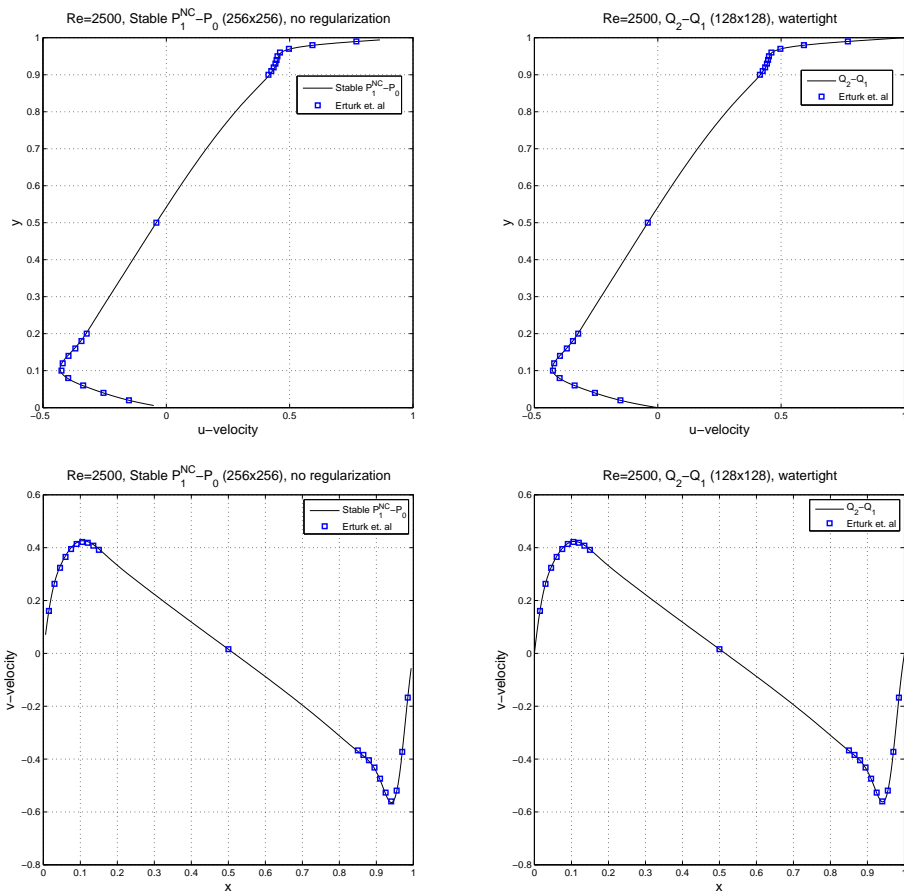
Figure 4.5: Profiles of u-velocity along the line $x = 0.5$ and v-velocity along $y = 0.5$ computed by using the stable P_1^{NC}-P_0 with unregularized boundary condition and Q_2-Q_1 with watertight boundary condition, Re $= 3200$.
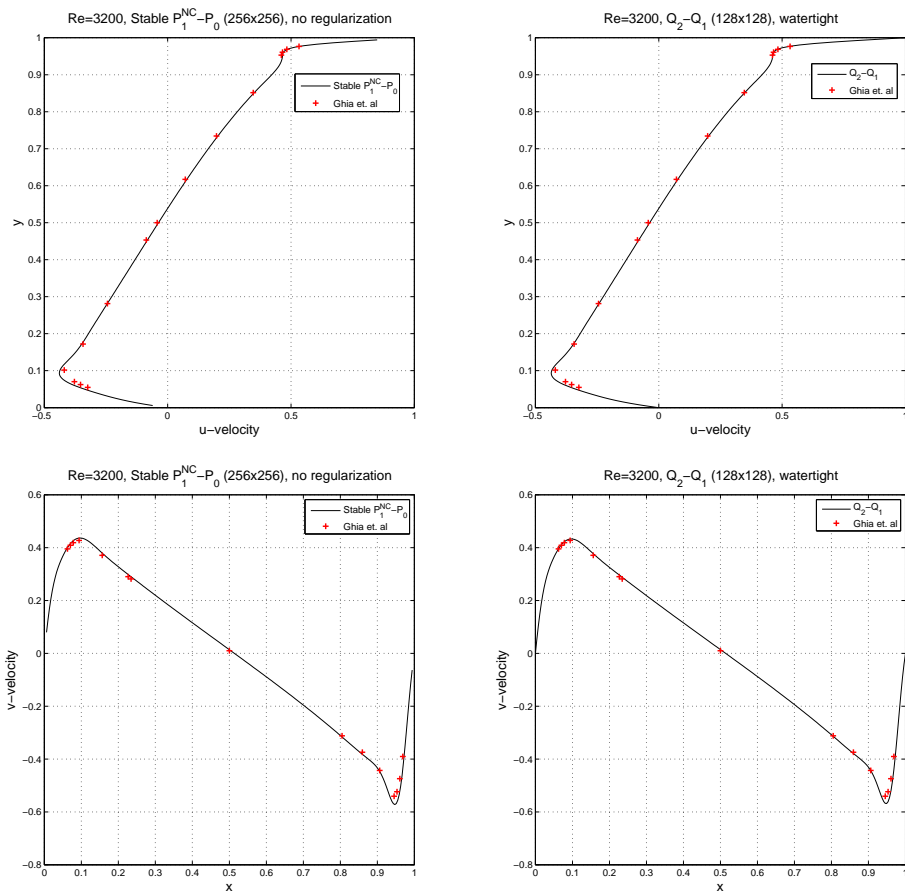
Figure 4.6: Profiles of u-velocity along the line $x = 0.5$ and v-velocity along $y = 0.5$ computed by using the stable P_1^{NC}-P_0 with unregularized boundary condition and Q_2-Q_1 with watertight boundary condition, Re $= 5000$.
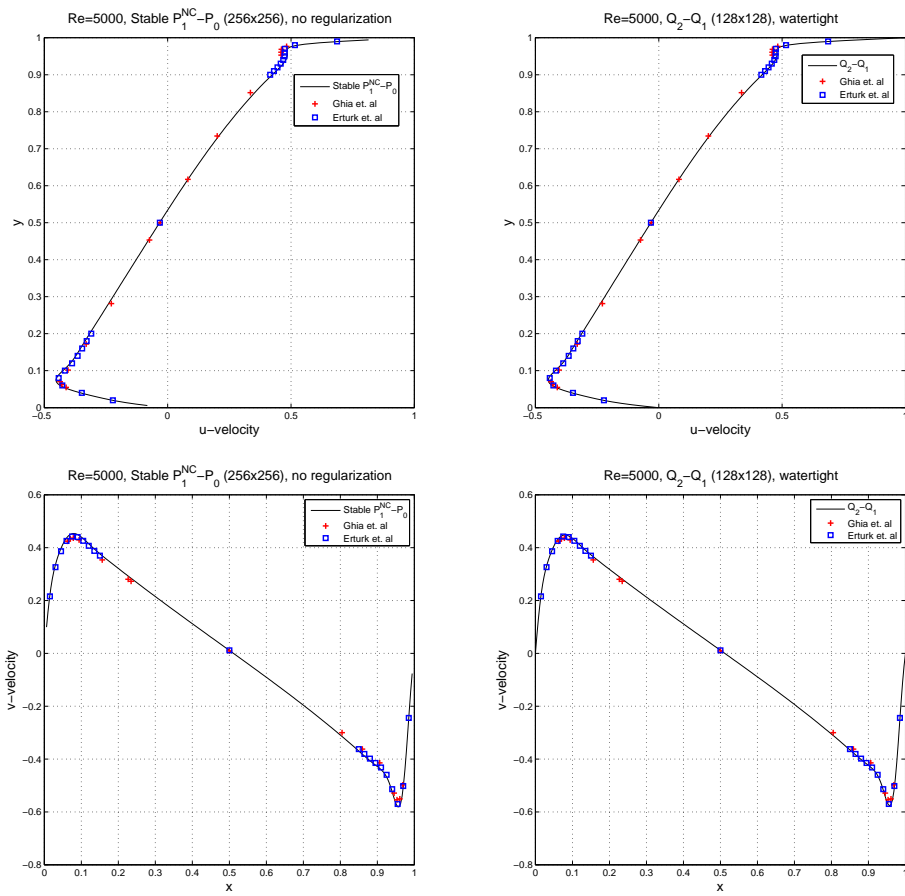
Table 4.12: Values used to plot the contours of the stream function, the vorticity and the pressure

Contours	Values
Stream function	-0.1175, -0.1150, -0.11, -0.1, -0.09, -0.07, -0.05, -0.03, -0.01, -1.0E-04, -1.0E-05, -1.0E-07, -1.0E-10, 1.0E-08, 1.0E-07, 1.0E-06, 1.0E-05, 5.0E-05, 1.0E-04, 2.5E-04, 5.0E-04, 1.0E-03, 1.5E-03, 3.0E-03
Vorticity	-5.0, -4.0, -3.0, -2.0, -1.0, -0.5, 0.0, 0.5, 1.0, 2.0, 3.0, 4.0, 5.0
Pressure	-0.1, -0.09, -0.08, -0.07, -0.06, -0.05, -0.04, -0.03, -0.02, -0.01, 0.0, 0.01, 0.02, 0.03, 0.04, 0.05, 0.06, 0.07, 0.08, 0.09, 0.1

We present computed streamlines in Figure 4.7–Figure 4.14 for Reynolds number from 100 to 5000. The figures of streamline contours computed by using the stable P_1^{NC}-P_0 with unregularized boundary condition are very much like those computed by using Q_2-Q_1 with watertight boundary condition. We present results of $\psi_{\max}$ and location of the centers of secondary vortices in Table 4.13–Table 4.15. The values of $\psi_{\max}$ and location of $\psi_{\max}$ computed by using both the stable P_1^{NC}-P_0 and Q_2-Q_1 show a good agreement compared with those in [19] and [42]. These figures in Figure 4.7–Figure 4.14 show that the primary vortex starts to move towards the cavity center as Reynolds number increases. We can observe that the counter-rotating secondary vortices at the bottom left and right. Both bottom left and right vortices grow in size as Reynolds number increases. Growth of the bottom right vortex is greater and its strength becomes greater than those of the bottom left vortex. It can be seen from Table 4.13 and Table 4.14. The secondary vortex at the top left is appeared as Reynolds number increases. It grows in size and strength as Reynolds number increases in Figure 4.11 and Table 4.15.

The vorticity contours are presented in Figure 4.15–Figure 4.17. We can observe that the gradient in vorticity is negligible in the center of cavity and the region of very low gradient in vorticity grows as Reynolds number increases. This shows that the fluid begins to rotate like a rigid body with constant

Figure 4.7: Streamline computed by using the stable P_1^{NC}-P_0 with unregularized boundary condition and Q_2-Q_1 with watertight boundary condition, Re = 100, 400.

Figure 4.8: Streamline computed by using the stable P_1^{NC}-P_0 with unregularized boundary condition and Q_2-Q_1 with watertight boundary condition, Re = 1000, 2500.

Figure 4.9: Streamline of bottom left vortex computed by using the stable P_1^{NC}-P_0 with unregularized boundary condition and Q_2-Q_1 with watertight boundary condition, Re = 1000, 2500.

Figure 4.10: Streamline of bottom right vortex computed by using the stable P_1^{NC}-P_0 with unregularized boundary condition and Q_2-Q_1 with watertight boundary condition, Re = 1000, 2500.
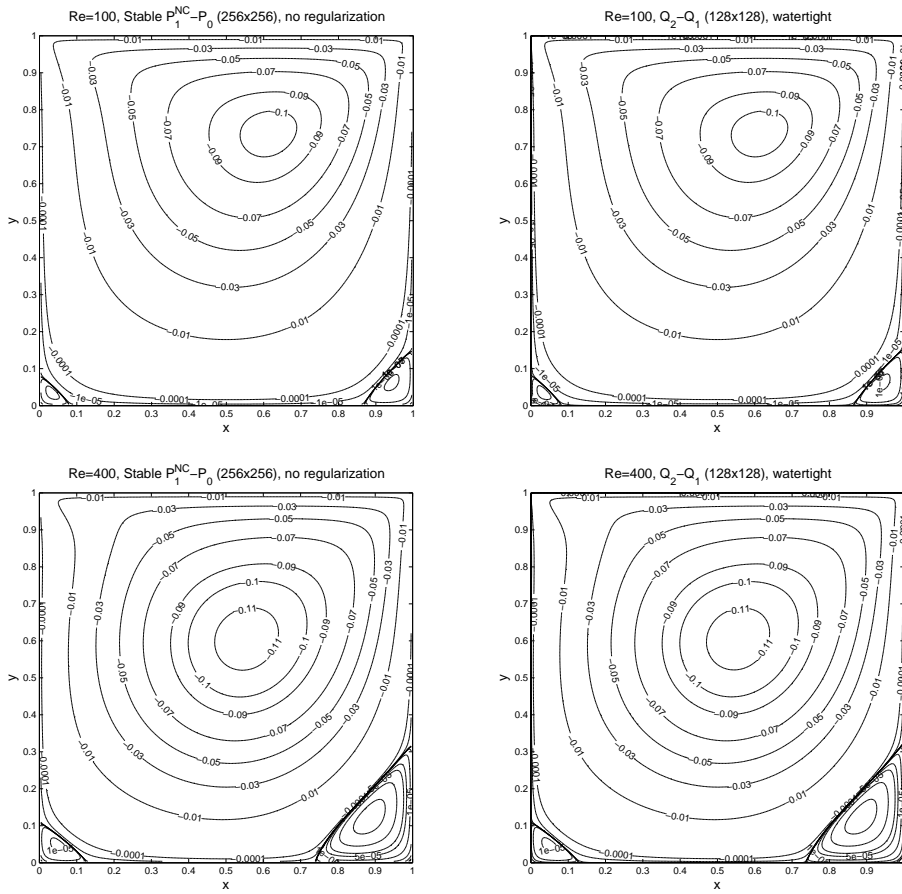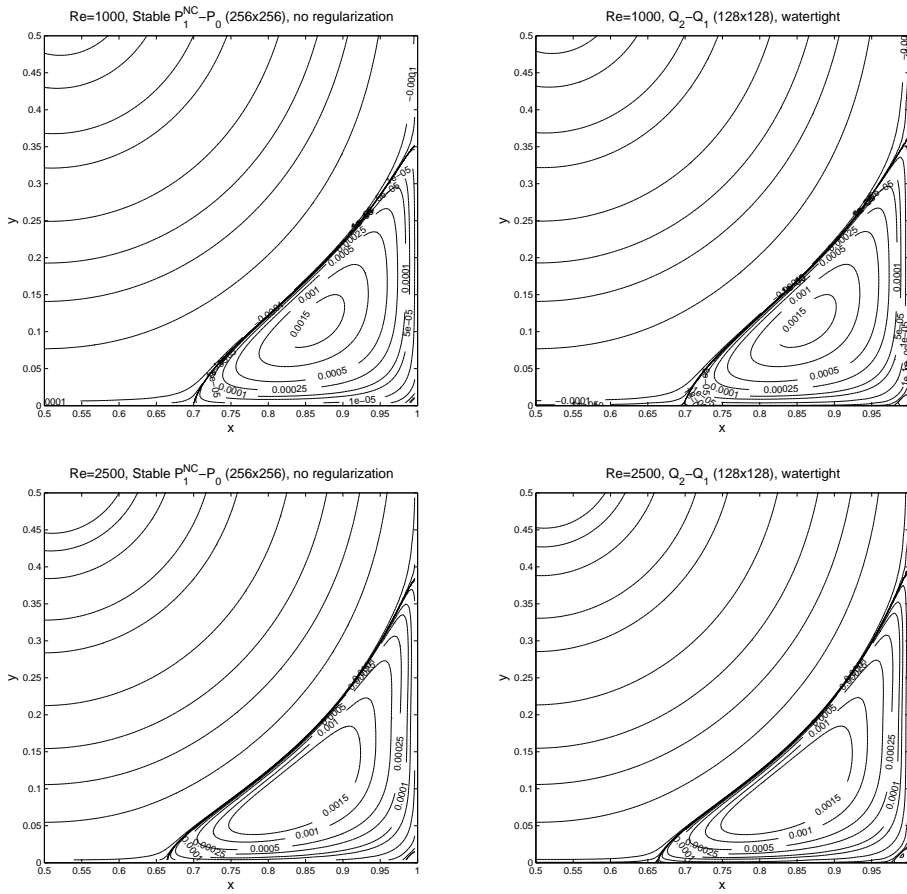
Figure 4.11: Streamline computed by using the stable P_1^{NC}-P_0 with unregularized boundary condition and Q_2-Q_1 with watertight boundary condition, Re = 3200, 5000.
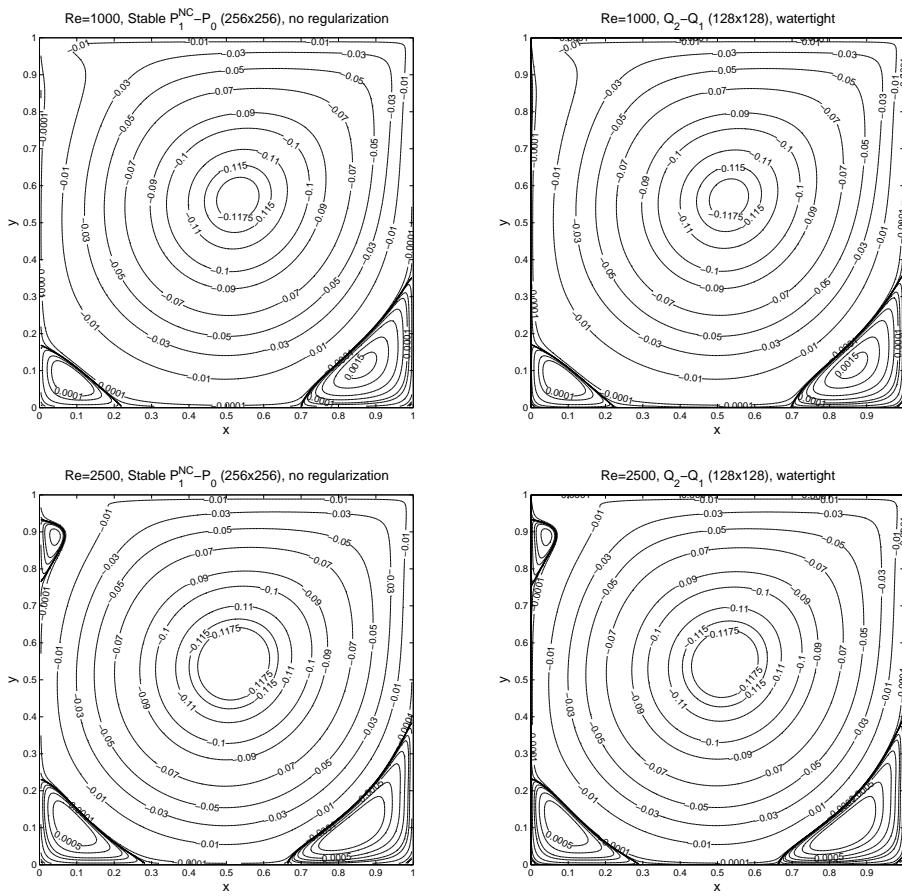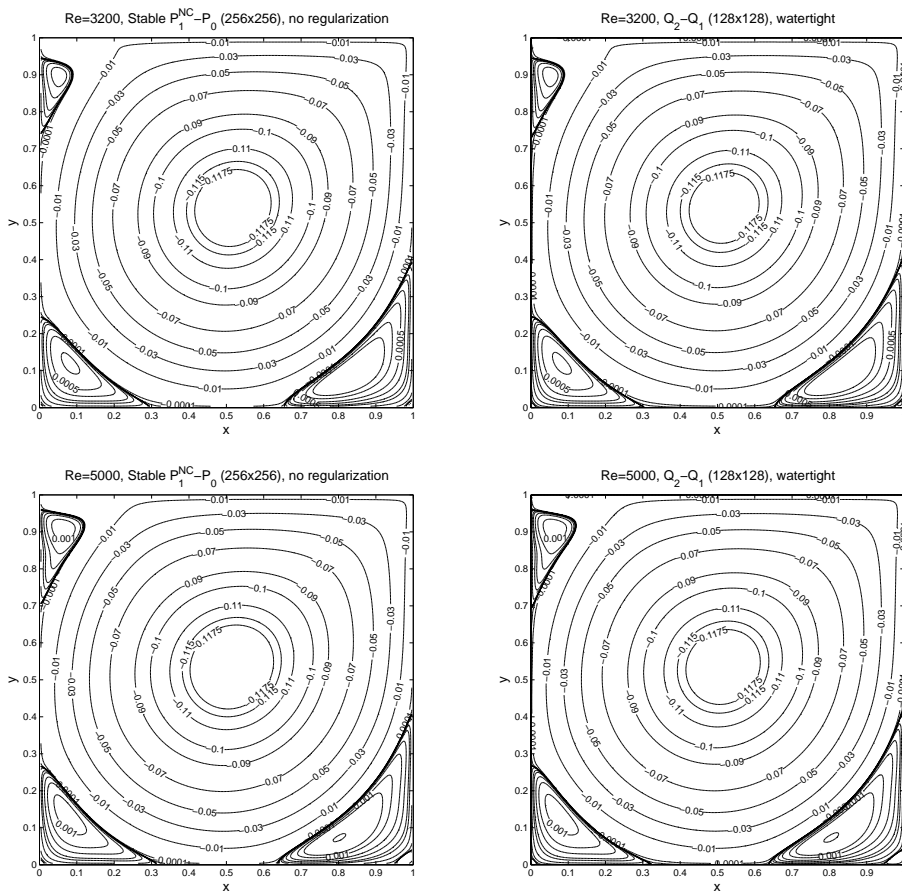
Figure 4.12: Streamline of bottom left vortex computed by using the stable P_1^{NC}-P_0 with unregularized boundary condition and Q_2-Q_1 with watertight boundary condition, Re = 3200, 5000.

Figure 4.13: Streamline of bottom right vortex computed by using the stable P_1^{NC}-P_0 with unregularized boundary condition and Q_2-Q_1 with watertight boundary condition, Re = 3200, 5000.
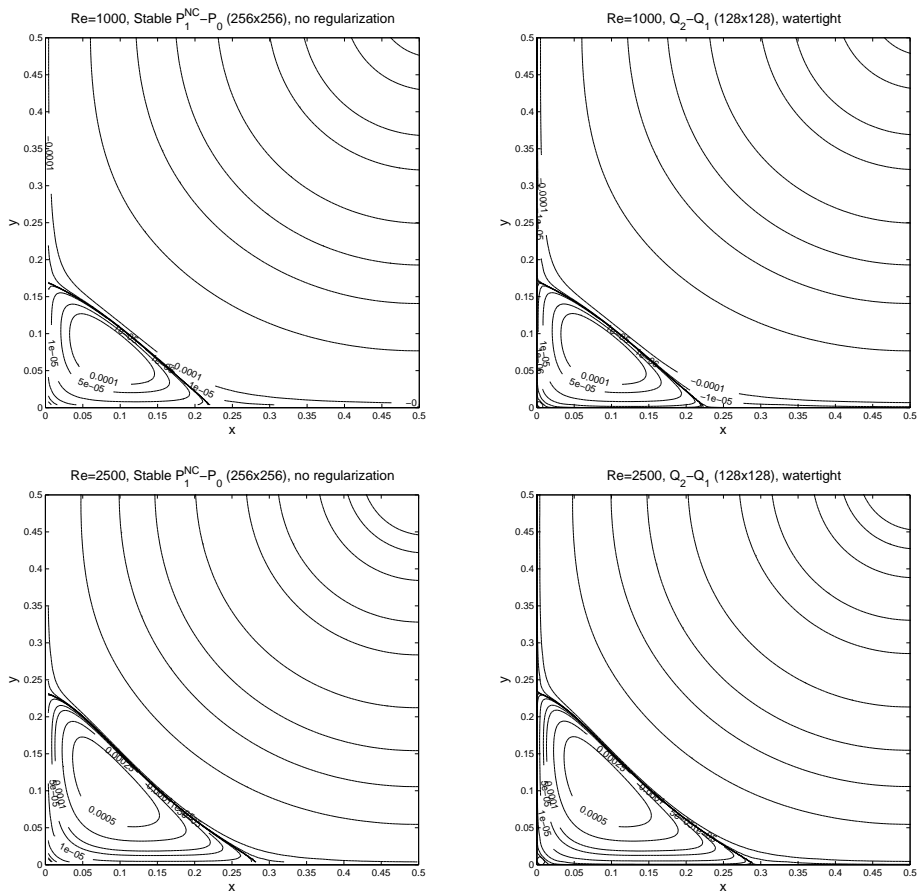

73

Figure 4.14: Streamline of top left vortex computed by using the stable P_1^{NC}-P_0 with unregularized boundary condition and Q_2-Q_1 with watertight boundary condition, Re = 3200, 5000.
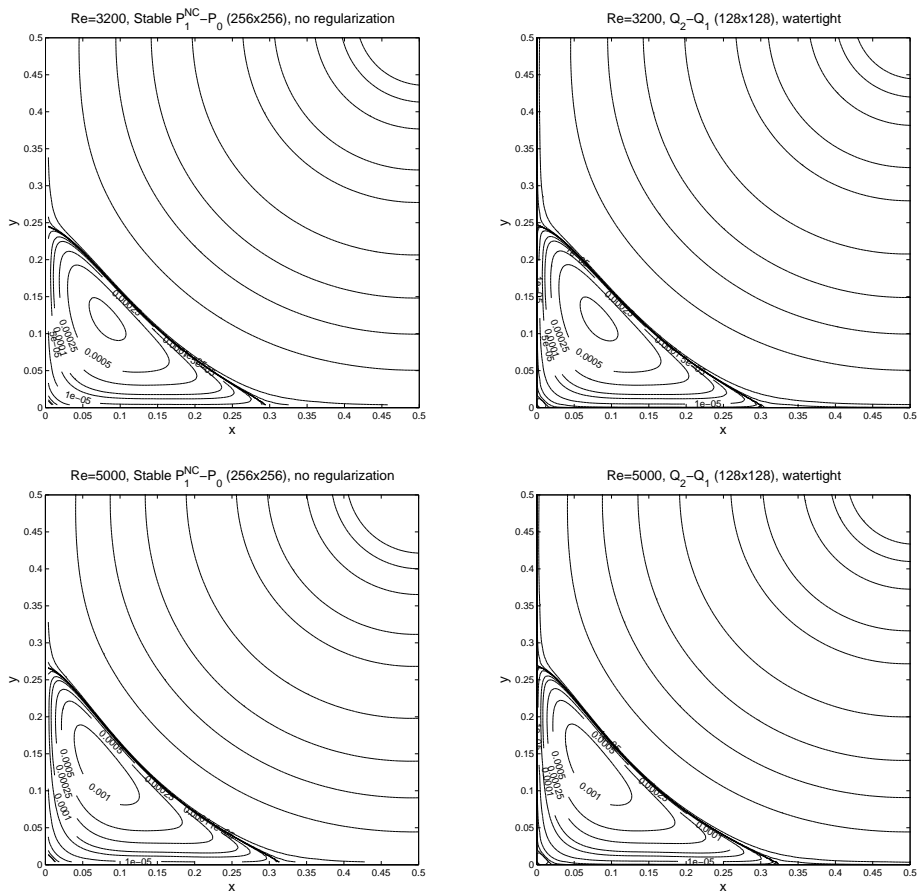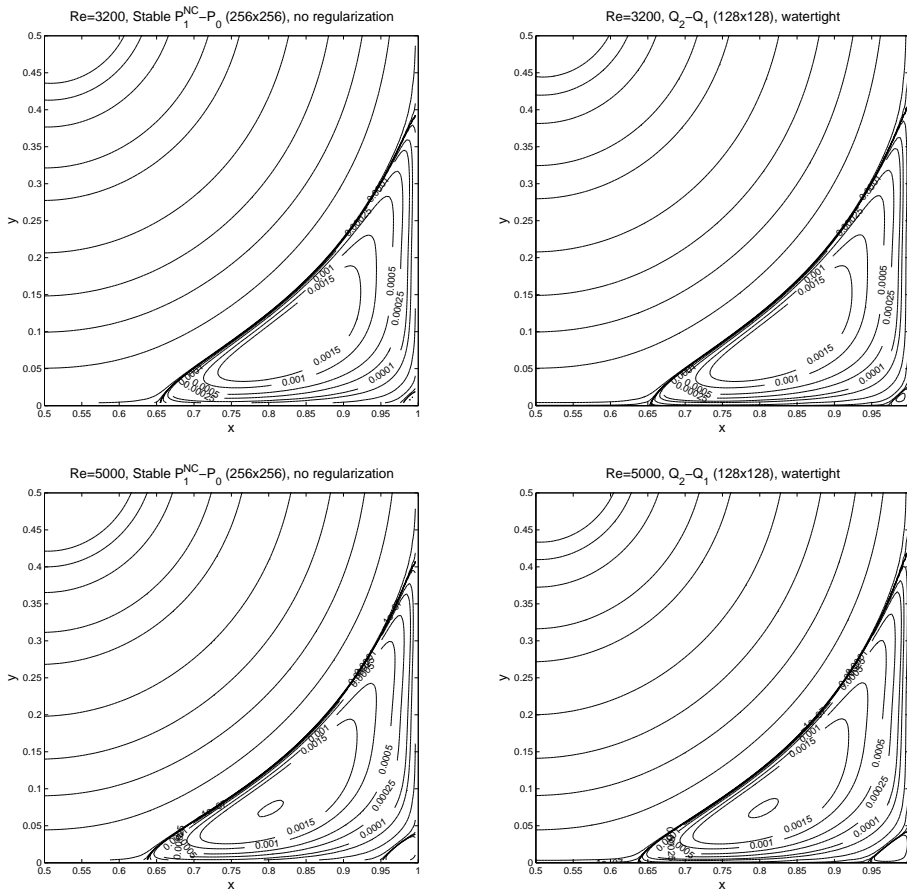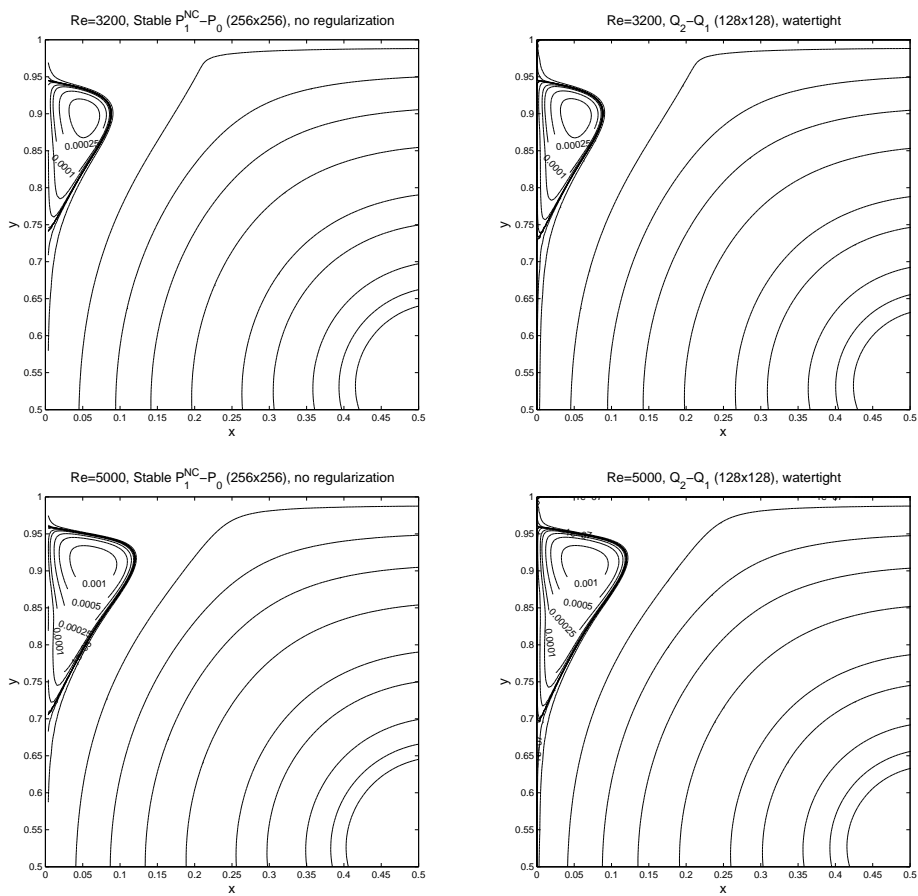
Table 4.13: $\psi_{\max}$ and location of the centers of bottom left vortex

	Grid	$\psi_{\max}$	(x,y)	Regularization
Re = 100				
P_1^{NC}-P_0	256×256	1.7368E-06	(0.0332,0.0332)	no
P_1^{NC}-P_0	256×256	1.7368E-06	(0.0332,0.0332)	(4.3)
Q_2-Q_1	128×128	3.0941E-07	(0.0273,0.0313)	leaky
Q_2-Q_1	128×128	1.7934E-06	(0.0352,0.0352)	watertight
Q_2-Q_1	128×128	1.7933E-06	(0.0352,0.0352)	(4.3)
[42]	257×257	1.7930E-06	(0.0332,0.0352)	[42]
Re = 400				
P_1^{NC}-P_0	256×256	1.4100E-05	(0.0488,0.0488)	no
P_1^{NC}-P_0	256×256	1.4101E-05	(0.0488,0.0488)	(4.3)
Q_2-Q_1	128×128	1.0052E-05	(0.0469,0.0469)	leaky
Q_2-Q_1	128×128	1.4329E-05	(0.0508,0.0469)	watertight
Q_2-Q_1	128×128	1.4330E-05	(0.0508,0.0469)	(4.3)
[42]	257×257	1.4272E-05	(0.0508,0.0461)	[42]
Re = 1000				
P_1^{NC}-P_0	256×256	2.3223E-04	(0.0840,0.0762)	no
P_1^{NC}-P_0	256×256	2.3193E-04	(0.0840,0.0762)	(4.3)
Q_2-Q_1	128×128	2.0364E-04	(0.0820,0.0781)	leaky
Q_2-Q_1	128×128	2.3337E-04	(0.0820,0.0781)	watertight
Q_2-Q_1	128×128	2.3312E-04	(0.0820,0.0781)	(4.3)
[42]	257×257	2.3301E-04	(0.0826,0.0776)	[42]
Re = 2500				
P_1^{NC}-P_0	256×256	9.2794E-04	(0.0840,0.1113)	no
P_1^{NC}-P_0	256×256	9.2503E-04	(0.0840,0.1113)	(4.3)
Q_2-Q_1	128×128	8.4410E-04	(0.0859,0.1094)	leaky
Q_2-Q_1	128×128	9.3084E-04	(0.0859,0.1094)	watertight
Q_2-Q_1	128×128	9.2841E-04	(0.0859,0.1094)	(4.3)
[19]	601×601	9.2541E-04	(0.0850,0.1100)	-
Re = 3200				
P_1^{NC}-P_0	256×256	1.1108E-03	(0.0801,0.1191)	no
P_1^{NC}-P_0	256×256	1.1068E-03	(0.0801,0.1191)	(4.3)
Q_2-Q_1	128×128	1.0141E-03	(0.0820,0.1172)	leaky
Q_2-Q_1	128×128	1.1151E-03	(0.0820,0.1172)	watertight
Q_2-Q_1	128×128	1.1116E-03	(0.0820,0.1172)	(4.3)
[42]	257×257	1.1121E-03	(0.0799,0.1203)	[42]
Re = 5000				
P_1^{NC}-P_0	256×256	1.3671E-03	(0.0723,0.1387)	no
P_1^{NC}-P_0	256×256	1.3611E-03	(0.0723,0.1387)	(4.3)
Q_2-Q_1	128×128	1.2489E-03	(0.0742,0.1328)	leaky
Q_2-Q_1	128×128	1.3782E-03	(0.0742,0.1367)	watertight
Q_2-Q_1	128×128	1.3710E-03	(0.0742,0.1367)	(4.3)
[42]	257×257	1.3689E-03	(0.0720,0.1382)	[42]

Table 4.14: $\psi_{\max}$ and location of the centers of bottom right vortex

	Grid	$\psi_{\max}$	(x, y)	Regularization
Re = 100				
P_1^{NC}-P_0	256×256	1.2597E-05	(0.9434,0.0605)	no
P_1^{NC}-P_0	256×256	1.2606E-05	(0.9434,0.0605)	(4.3)
Q_2-Q_1	128×128	7.4329E-06	(0.9453,0.0586)	leaky
Q_2-Q_1	128×128	1.2705E-05	(0.9414, 0.0625)	watertight
Q_2-Q_1	128×128	1.2715E-05	(0.9414, 0.0625)	(4.3)
[42]	257×257	1.2658E-05	(0.9424,0.0610)	[42]
Re = 400				
P_1^{NC}-P_0	256×256	6.4495E-04	(0.8848,0.1230)	no
P_1^{NC}-P_0	256×256	6.4515E-04	(0.8848,0.1230)	(4.3)
Q_2-Q_1	128×128	5.8921E-04	(0.8867,0.1211)	leaky
Q_2-Q_1	128×128	6.4393E-04	(0.8867,0.1250)	watertight
Q_2-Q_1	128×128	6.4415E-04	(0.8867,0.1250)	(4.3)
[42]	257×257	6.6404E-04	(0.8835,0.1203)	[42]
Re = 1000				
P_1^{NC}-P_0	256×256	1.7319E-03	(0.8652,0.1113)	no
P_1^{NC}-P_0	256×256	1.7299E-03	(0.8652,0.1113)	(4.3)
Q_2-Q_1	128×128	1.6103E-03	(0.8672,0.1133)	leaky
Q_2-Q_1	128×128	1.7286E-03	(0.8633,0.1133)	watertight
Q_2-Q_1	128×128	1.7267E-03	(0.8633,0.1133)	(4.3)
[42]	257×257	1.7240E-03	(0.8658,0.1119)	[42]
Re = 2500				
P_1^{NC}-P_0	256×256	2.6662E-03	(0.8340,0.0918)	no
P_1^{NC}-P_0	256×256	2.6598E-03	(0.8340,0.0918)	(4.3)
Q_2-Q_1	128×128	2.4696E-03	(0.8359,0.0898)	leaky
Q_2-Q_1	128×128	2.6621E-03	(0.8320,0.0898)	watertight
Q_2-Q_1	128×128	2.6560E-03	(0.8320,0.0898)	(4.3)
[19]	601×601	2.6561E-03	(0.83505,0.0917)	-
Re = 3200				
P_1^{NC}-P_0	256×256	2.8326E-03	(0.8223,0.0840)	no
P_1^{NC}-P_0	256×256	2.8246E-03	(0.8223,0.0840)	(4.3)
Q_2-Q_1	128×128	2.6157E-03	(0.8281,0.0859)	leaky
Q_2-Q_1	128×128	2.8292E-03	(0.8242,0.0859)	watertight
Q_2-Q_1	128×128	2.8217E-03	(0.8242,0.0859)	(4.3)
[42]	257×257	2.8234E-03	(0.8259,0.0847)	[42]
Re = 5000				
P_1^{NC}-P_0	256×256	3.0653E-03	(0.8027,0.0723)	no
P_1^{NC}-P_0	256×256	3.0541E-03	(0.8027,0.0723)	(4.3)
Q_2-Q_1	128×128	2.8099E-03	(0.8086,0.0742)	leaky
Q_2-Q_1	128×128	3.0765E-03	(0.8047,0.0742)	watertight
Q_2-Q_1	128×128	3.0640E-03	(0.8047,0.0742)	(4.3)
[42]	257×257	3.0651E-03	(0.8081,0.0741)	[42]

Table 4.15: $\psi_{\max}$ and location of the centers of top left vortex

	Grid	$\psi_{\max}$	(x, y)	Regularization
Re = 2500				
P_1^{NC}-P_0	256×256	3.3939E-04	(0.0410,0.8887)	no
P_1^{NC}-P_0	256×256	3.5485E-04	(0.0449,0.8926)	(4.3)
Q_2-Q_1	128×128	4.1818E-05	(0.0352,0.8789)	leaky
Q_2-Q_1	128×128	3.4219E-04	(0.0430,0.8906)	watertight
Q_2-Q_1	128×128	3.5718E-04	(0.0430,0.8906)	(4.3)
[19]	601×601	3.4455E-04	(0.0433,0.8900)	-
Re = 3200				
P_1^{NC}-P_0	256×256	7.0799E-04	(0.0527,0.9004)	no
P_1^{NC}-P_0	256×256	7.2547E-04	(0.0527,0.9004)	(4.3)
Q_2-Q_1	128×128	2.7067E-04	(0.0469,0.8945)	leaky
Q_2-Q_1	128×128	7.0781E-04	(0.0547,0.8984)	watertight
Q_2-Q_1	128×128	7.2466E-04	(0.0547,0.9023)	(4.3)
[42]	257×257	7.0580E-04	(0.0530,0.8984)	[42]
Re = 5000				
P_1^{NC}-P_0	256×256	1.4582E-03	(0.0645,0.9082)	no
P_1^{NC}-P_0	256×256	1.4680E-03	(0.0645,0.9121)	(4.3)
Q_2-Q_1	128×128	8.2649E-04	(0.0586,0.9063)	leaky
Q_2-Q_1	128×128	1.4477E-03	(0.0625,0.9102)	watertight
Q_2-Q_1	128×128	1.4511E-03	(0.0625,0.9102)	(4.3)
[42]	257×257	1.4383E-03	(0.0621,0.9108)	[42]

angular velocity [42].

The contours of pressure fields are presented in Figure 4.18–Figure 4.20. It can be seen that the regions of high gradient in pressure become smaller at the top left and right corner in the cavity as Reynolds number increases. Especially, the regions of high gradient in pressure at the top left corner is negligible when Re $= 5000$.

The figures of vorticity and pressure fields contours computed by using the stable P_1^{NC}-P_0 with unregularized boundary condition are very much like those computed by using Q_2-Q_1 with watertight boundary condition. These vorticity and pressure contours are well known in the literature, for example those in [23].

Figure 4.15: Contours of vorticity computed by using the stable P_1^{NC}-P_0 with unregularized boundary condition and Q_2-Q_1 with watertight boundary condition, Re = 100, 400.
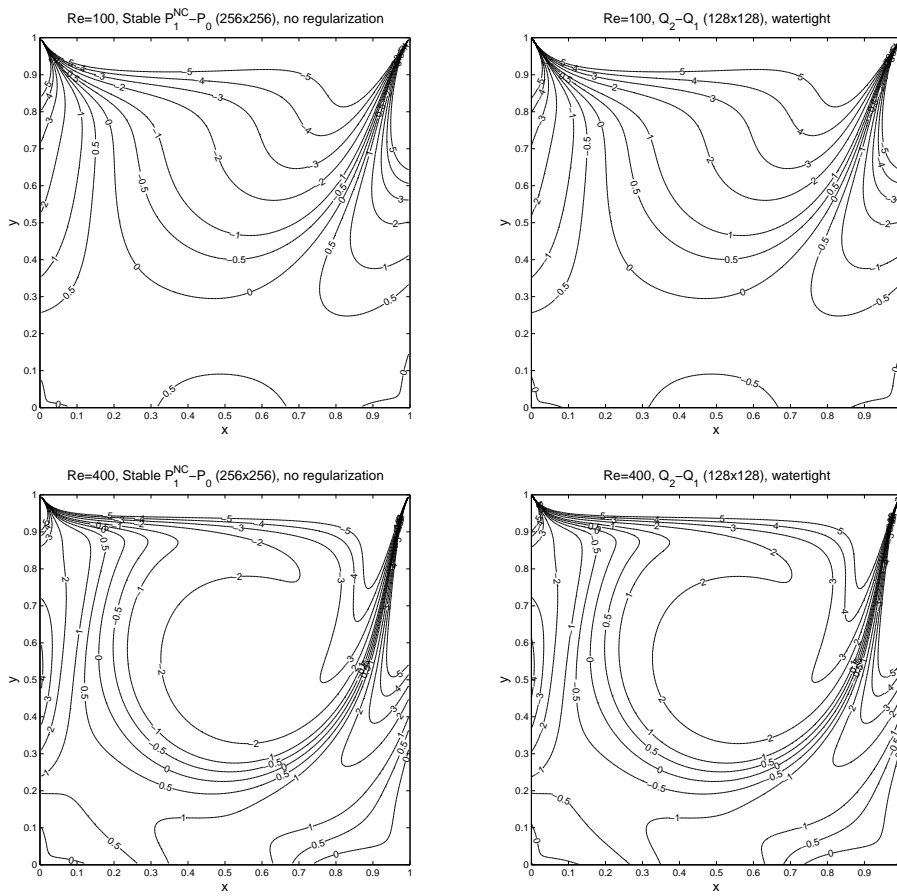
Figure 4.16: Contours of vorticity computed by using the stable P_1^{NC}-P_0 with unregularized boundary condition and Q_2-Q_1 with watertight boundary condition, Re = 1000, 2500.
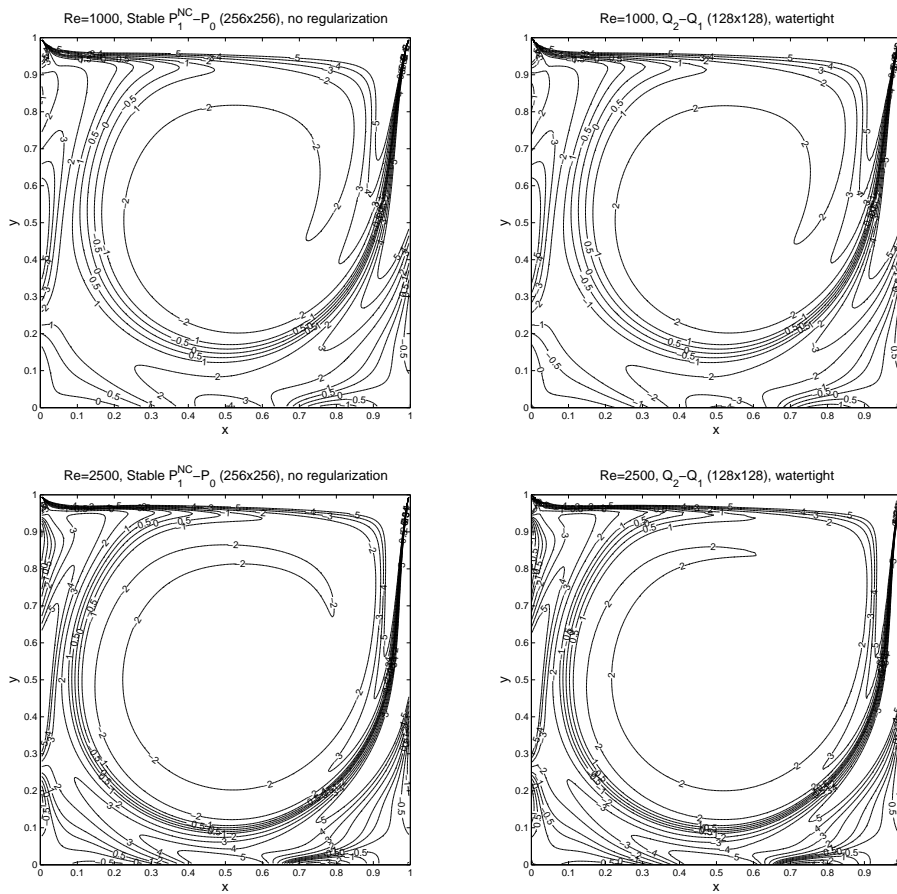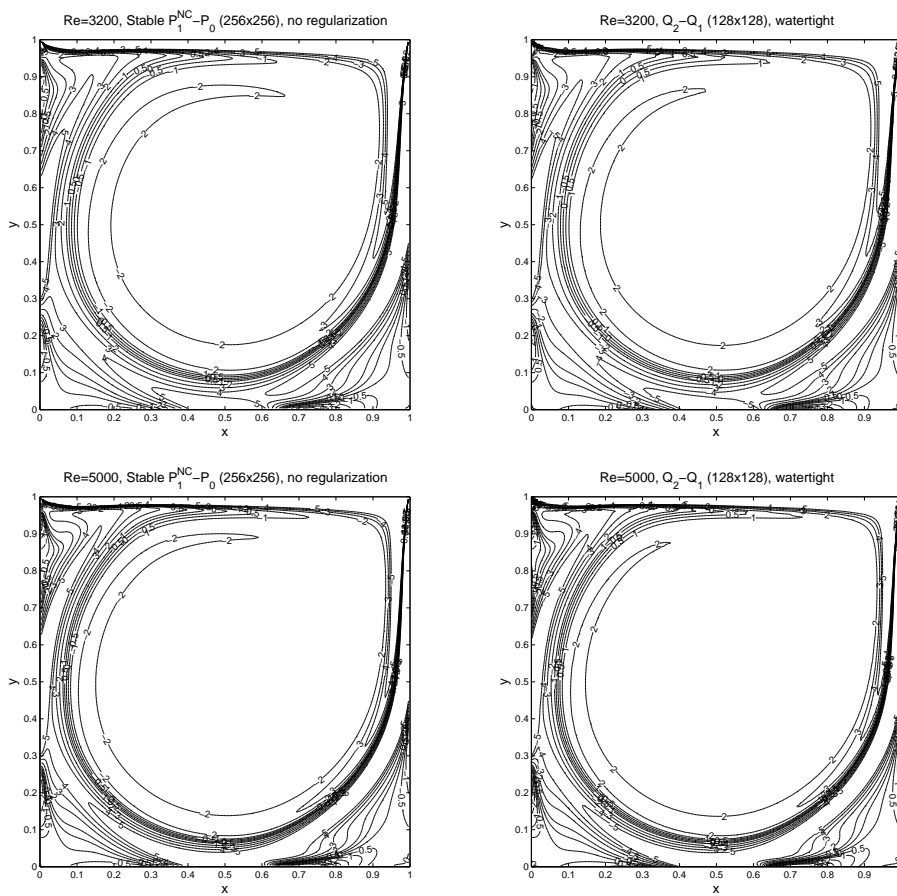
Figure 4.17: Contours of vorticity computed by using the stable P_1^{NC}-P_0 with unregularized boundary condition and Q_2-Q_1 with watertight boundary condition, Re = 3200, 5000.
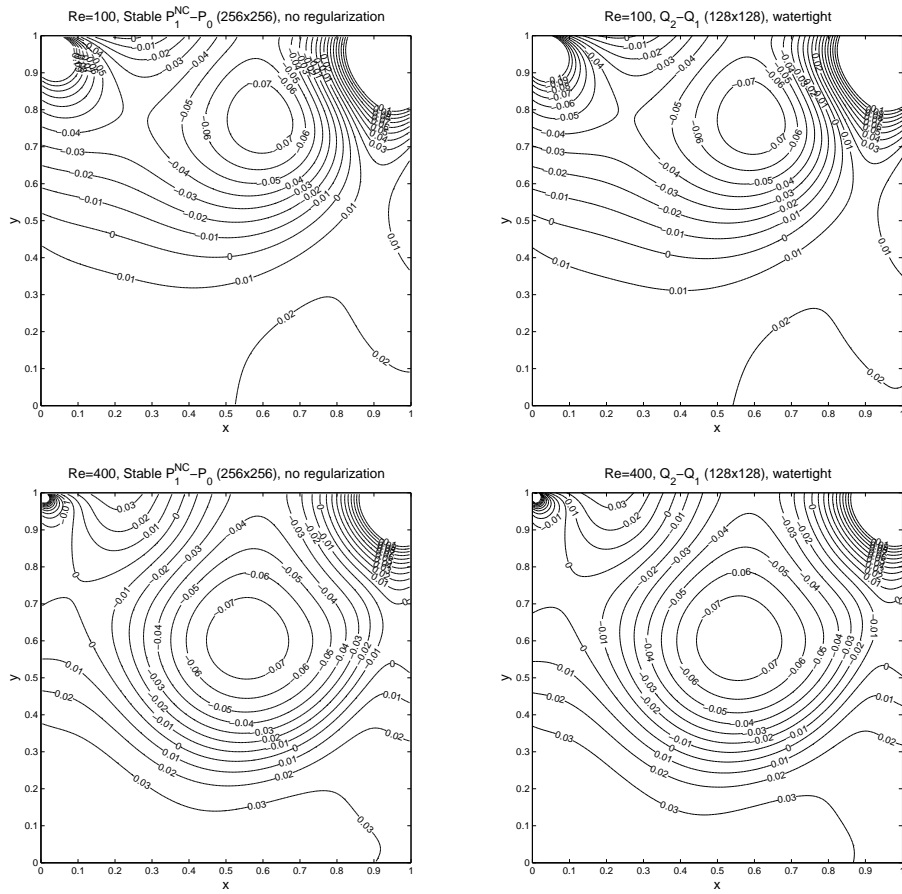
Figure 4.18: Contours of pressure fields computed by using the stable P_1^{NC}-P_0 with unregularized boundary condition and Q_2-Q_1 with watertight boundary condition, Re = 100, 400.

Figure 4.19: Contours of pressure fields computed by using the stable P_1^{NC}-P_0 with unregularized boundary condition and Q_2-Q_1 with watertight boundary condition, Re = 1000, 2500.
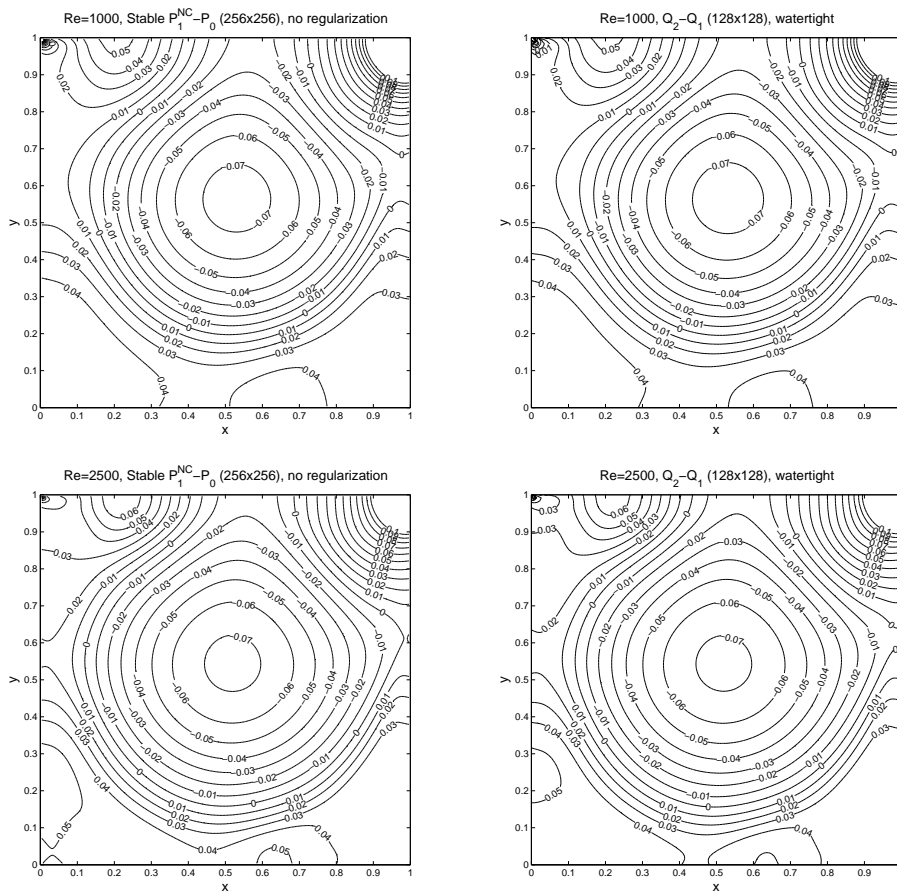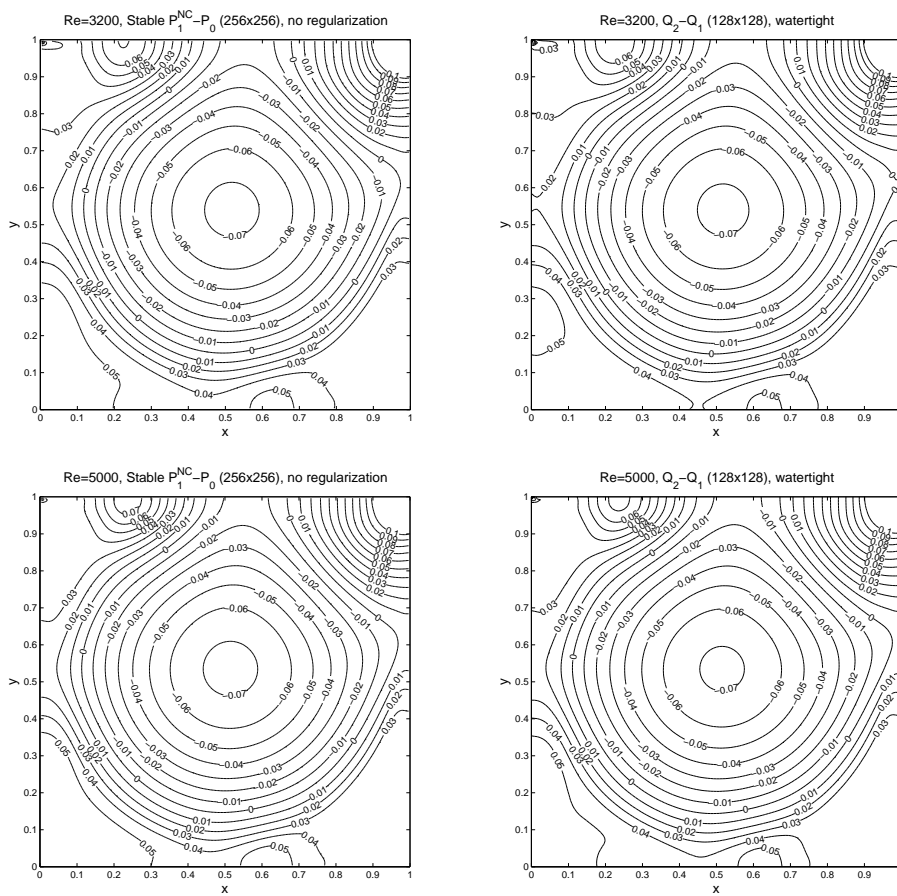
Figure 4.20: Contours of pressure fields computed by using the stable P_1^{NC}-P_0 with unregularized boundary condition and Q_2-Q_1 with watertight boundary condition, Re = 3200, 5000.

Chapter 5

Conclusion

This thesis has attempted to solve the incompressible flow in a square cavity without smoothing singularities at the top corners of the cavity. Since P_1^{NC} is to employ the degrees of freedom associated with values at the mid points of edges, it is not required to impose the values at the vertices. By using this property, P_1^{NC}-P_0 is possible to solve the lid driven cavity problem without modification of boundary condition on the top of the cavity. In implementation of the P_1^{NC}-P_0 for solving the lid driven cavity problem, P_1^{NC} is not enough to approximate the unregularized boundary condition on the top of cavity. DSSY nonconforming finite element has been introduced to approximate the the boundary condition on the top of the cavity. By adding DSSY finite element to the elements which are on the top corners in the cavity, it is possible to approximate the unregularized boundary condition on the top of the cavity sufficiently. Numerical solutions have been computed by using the stable P_1^{NC}-P_0 with and without modification of boundary condition. Numer-

ical solutions have been computed by using conforming Q_2-Q_1 finite elements with a leaky, watertight, and regularized boundary conditions for the purpose of comparison. Three indicators for accuracy of the numerical solution have been presented. The incompressible condition for a fluid and compatibility condition for the Poisson equation for the stream function with the Neumann boundary condition are used to check the accuracy of the numerical solutions. Our numerical solutions computed by using both the stable P_1^{NC}-P_0 and Q_2-Q_1 are in good agreement with those in the literature except in the case of the numerical solutions computed by using Q_2-Q_1 with leaky cavity boundary condition. And our numerical solutions satisfy the incompressible and compatibility condition precisely. Numerical results computed by using the stable P_1^{NC}-P_0 with unregularized boundary conditions show the best results in terms of satisfying incompressible and compatibility conditions.

Bibliography

[1] F. Auteri, N. Parolini, and L. Quartapelle. Numerical investigation on the stability of singular driven cavity flow. *Journal of Computational Physics*, 183:1–25, 2002.

[2] M. Aydin and R. Fenner. Boundary element analysis of driven cavity flow for low and moderate Reynolds number. *International Journal for Numerical Methods in Fluids*, 37:45–64, 2001.

[3] I. Babuška. The finite element method with Lagrange multipliers. *Numerische Mathematik*, 20:179–192, 1973.

[4] R. E. Bank, B. D. Welfert, and H. Yserentant. A class of iterative methods for solving saddle point problems. *Numerische Mathematik*, 56:645–666, 1990.

[5] E. Barragy and G. Carey. Stream function-vorticity driven cavity solution using p finite elements. *Computers & Fluids*, 26:453–468, 1997.

[6] O. Botella and R. Peyret. Benchmark spectral results on the lid-driven cavity flow. Computers & Fluids, 27:421–433, 1998.

[7] O. Botella and R. Peyret. Computing singular solutions of the Navier-Stokes equations with the Chebyshev collocation method. *International Journal for Numerical Methods*, 36:125–163, 2001.

[8] Dietrich Braess. Finite elements: Theory, fast solvers, and applications in solid mechanics. Cambridge University Press, Cambridge, 3rd edition, 2007.

[9] J. H. Bramble, J. E. Pasciak, and A. T. Vassilev. Analysis of the inexact Uzawa algorithm for saddle point problems. *SIAM Journal on Numerical Analysis*, 34:1072–1092.

[10] A. Brandt. Algebraic multigrid theory: the symmetric case. *Applied Mathematics and Computation*, 19:23–56, 1986

[11] A. Brandt, S. F. McCormick, and J. Ruge. Algebraic multigrid (AMG) for automatic multigrid solution with application to geodetic computations. Institute for Computational Studies, POB 1852, Fort Collins, Colorado, 1982.

[12] F. Brezzi. On the existence, uniqueness approximation of saddle-point problems arising from Lagrange multipliers. *R.A.R.I.O. Analyse Numerique*, 8:129–151, 1974.

[13] C. Bruneau and M. Saad The 2D lid-driven cavity problem revisited. *Computers & Fluids*, 35:326–348, 2006.

[14] W. Briggs, V. Henson, and S. McCormic. A multigrid tutorials. Society for Industrial and Applied Mathematics, Philadelphia, 2000.

[15] M. Crouzeix and P.-A. Raviart. Conforming and nonconforming finite element methods for solving the stationary Stokes equations. *R.A.R.I.O. Analyse Numerique*, 7:33–75, 1973.

[16] J. Douglas, Jr., J. E. Santos, D. Sheen, and X. Ye. Nonconforming Galerkin methods based on quadrilateral elements for second order elliptic problems. *ESAIM–Math. Model. Numer. Anal.*, 33(4):747–770, 1999.

[17] H. Elman. Preconditioning for the steady-state Navier-Stokes equations with low viscosity. *SIAM Journal on Scientific Computing*, 20:1299-1316, 1999.

[18] H. Elman, D. Silvester, and A. Wathen. Finite elements and fast iterative solvers: with applications in incompressible fluid dynamics. Oxford University Press, Oxford, 2005.

[19] E. Erturk, T. C. Corke, and C. Gökçöl. Numerical solutions of 2-D steady incompressible driven cavity flow at high Reynolds numbers. *International Journal for Numerical Methods in Fluids*, 48:747–774, 2005.

[20] P. Gervasio, F. Saleri, and A. Veneziani. Algebraic fractional-step schemes with spectral methods for the incompressible Navier-Stokes equations. *Journal of Computational Physics*, 214:347–365, 2006.

[21] U. Ghia, K. N. Ghia, and C. T. Shin. High-Re solutions for incompressible flow using the Navier-Stokes equations and a multigrid method. *Journal of computational physics*, 48:387–411, 1982.

[22] V. Girault and P.-A. Raviart. Finite elements methods for the Navier-Stokes equations. Springer, Heidelberg, 1986.

[23] R. Glowinski. Finite element methods for incompressible viscous flow, in P. G. Ciarlet, J. L. Lions (Eds.), Handbook of Numerical Analysis, vol. IX. North Holland, Amsterdam, 2003.

[24] O. Goyon. High-Reynolds number solutions of Navier-Stokes equations using incremental unknowns. *Computer Methods in Applied Mechanics and Engineering*, 130:319–335, 1996.

[25] M. Gupta and R. Manohar. Boundary approximations and accuracy in viscous flow computation. *Journal of Computational Physics*, 31:265–288, 1979.

[26] M. Gupta and J. Kalita A new paradigm for solving Navier-Stokes equations: streamfunction-velocity formulation *Journal of Computational Physics*, 207:52–68, 2005.

[27] W. Hackbusch. Multi-grid methods and applications Springer-Verlag, Berlin, 1985

[28] W. Hackbusch. Iterative solution of large sparse systems of equations. Springer-Verlag, Berlin, 1994

[29] S. Hou, Q. Zou, S. Chen, G. Doolen, and A. Cogley Simulation of cavity flow by the Lattice Boltzmann method. *Journal of Computational Physics*, 118:329–347, 1995

[30] O. Karakashian. On a Galerkin-Lagrangian multiplier method for the stationary Navier-Stokes equations. *SIAM Journal on Numerical Analysis*, 19:909–923, 1982.

[31] P. Hood and C. Taylor. A numerical solution of the Navier-Stokes equations using the finite element techniques. *Computers and Fluids*, 1:73–100,1973.

[32] S. Kim, D. Sheen, and J. Yim. A stable cheapest nonconforming finite element for the stationary Stokes equations. To be submitted.

[33] M. F. Murphy, G. H. Golub, and A. J. Wathen. A note on preconditioning for Indefinite linear system. *SIAM Journal on Scientific Computing*, 21:1969–1972, 2000.

[34] H. Nam, H. Choi, C. Park, and D. Sheen. A cheapest nonconforming rectangular finite element for the stationary Stokes problem. *Computer Methods in Applied Mechanics and Engineering*, 257:77–86, 2013.

[35] M. Henriksen and J. Holmen. Algebraic splitting for incompressible Navier-Stokes equations. *Journal of Computational Physics*, 175:438–453, 2002.

[36] `http://www.cs.umd.edu/~elman/ifiss`

[37] C. Park and D. Sheen. P_1-nonconforming quadrilateral finite element methods for second-order elliptic problems. *SIAM Journal on Numerical Analysis*, 41:624–640, 2003.

[38] R. Rannacher and S. Turek. Simple nonconforming quadrilateral Stokes element. *Numerical Methods for Partial Differential Equations*, 8:97–111, 1992.

[39] J. Ruge and K. Stüben. Algebraic multigrid (AMG). In S. McCormick editor, Multigrid methods, volume 5 of Frontiers in Applied Mathematics, 73–130, Society for Industrial and Applied Mathematics, 1986.

[40] Y. Saad. Iterative methods for sparse linear systems. Society for Industrial and Applied Mathematics, 2nd edition, 2003.

[41] Y. Sadd and M. H. Schultz. GMRES: A generalized minimum residual algorithm for solving nonsymmetric linear systems. *SIAM Journal on Scientific and Statistical Computing*, 7:856–869, 1986.

[42] M. Sahin and R. Owens. A novel fully implicit finite volume methods applied to the lid-driven cavity problem-Part I: High Reynolds number flow calculations. *International Journal for Numerical Methods in Fluids*, 42:57–77, 2003.

[43] J. Schöberl and W. Zulehner. On Schwarz-type smoothers for saddle point problems. *Numerische Mathematik*, 95:377–399, 2003.

[44] J. Shen. Hopf bifurcation of the unsteady regularized driven cavity flow. *Journal of Computational Physics*, 95:228–245, 1991.

[45] K. Stüben. An introduction to algebraic multigrid. In U. Trottenberg, C. Oosterlee, and A. Schüller, editors, Multigrid, 413–532. Academic Press, London, 2001.

[46] K. Stüben. A review of algebraic multigrid. *Journal of Computational and Applied Mathematics*, 128:281–309, 2001.

[47] U. Trottenberg and C. Oosterlee, and A. Schüller. Multigrid. Academic Press, London, 2001.

[48] H. A. Van der Vorst. Bi-CGstab: A fast and smoothly converging variant of Bi-CG for the solution of nonsymmetric linear systems. *SIAM Journal on Scientific and Statistical Computing*, 13:631–644, 1992.

국문초록

　　본 논문에서는 공동 구조 속의 비압축 유동 문제를 풀 때, 공동 위쪽 양 끝에 존재하는 특이점을 조정하지 않고 수치해를 구할 수 있는 방법을 제시하였다. 비순응 유한 요소법은 유한 요소 끝 점에서 자유도가 부여되지 않으므로, 공동 위쪽 양 끝점에서의 값을 고려하지 않아도 된다. 이 때문에 비순응 유한요소를 이용하면 원래 문제를 수정하지 않고도 정밀한 수치해를 구할 수 있다. 비압축 유동 문제를 풀 때 안정 비순응 P_1-P_0를 사용하였다. 공동 위쪽의 경계 조건을 정확하게 근사하기 위해, 공동 위쪽 양 끝에 있는 유한 요소에 DSSY 비순응 유한 요소를 더하였다. 비교를 위해 순응 유한 요소를 이용하여 수치해를 구하였다. 다른 연구에서 제시한 수치해와 비교하여 이 논문에서 구한 수치해를 검증하였고, 정확한 해를 구하였음을 확인하였다. 특히 안정 비순응 P_1-P_0를 사용하여 구한 수치해가 매우 정밀한 것을 알 수 있었다.